



Study of Electrical Conductivity of Thin Films with Near-Field Scanning Microwave Microscopy

Amanda Rachael de Souza (A0071160W)

April 5, 2014

A Thesis Submitted in Partial Fulfilment for the Requirements for the Degree of Bachelor of
Science with Honours

Supervised by: Professor ONG Chong Kim

Department of Physics, Faculty of Science

National University of Singapore, 2014

Acknowledgements

This thesis would not have been possible without a group of very important people and with deepest gratitude, I dedicate this to you.

To **Professor Ong Chong Kim**, for your dedication and patient guidance as my supervisor. I have learnt a lot under your supervision and am inspired by your enthusiasm and unending thirst for knowledge and progress in your field of physics. Thank you for the advice you have given me time and time again and for being a great teacher to me.

To **Dr. Wu Zhe**, for your time and encouragement as my mentor in the CSMM lab. Thank you for your patience in answering all my questions and for guiding me along the course of this project. I have learnt much of the things I know because you took the time to explain it to me and I really appreciate that.

To **everyone in the CSMM Lab group**, especially **Sun Weiqiang** and **Shawn Tang**, for graciously helping me in one way or another when I needed assistance.

To **my physics classmates**, for the times we've spent together in and out of class. Thank you for being my funny companions the past 4 years. You have shown me that our friendship is more important than your grades in tirelessly explaining concepts or homework questions to me and never hesitating to share your knowledge. I am only here today because of you guys and girls and I am truly grateful to have been allowed to share this experience with you.

To **all my friends**, for sharing your lives with me and for letting me share mine with you. Thank you for the years of friendship and for individually being there for me when I needed someone to pick me up when I fall, to put a smile on my face or to hold my hand. To **Charmaine, Jollyn, Samantha, Kirsten** and no least, **Jonathan**, I cannot thank you enough for being my pillars of strength and for standing by me no matter what. I am who I am today because of you and I am truly blessed to have you in my life. You will always and always have a special place in my heart.

To **my family**, for your unconditional love and care all these years. Thank you for being so generous of yourselves and for sacrificing so much to bring me up and to support me in all my endeavours. From the bottom of my heart, I am truly proud to have you as my family and I hope I will continue to do you proud always.

Abstract

Near-field scanning microwave microscopy (NSMM) is a tool for characterization at microwave frequencies. The NSMM system design used consists of a sharpened metal tip, mounted on the centre conductor of a high quality (Q) $\lambda/4$ coaxial resonator with microwave energy supplied from a Vector Network Analyzer (VNA) connected to the setup.

The measurement data is acquired in the form of a shift in resonant frequency f_r and a quality factor Q change when the resonator and probe tip is held above a sample. Using a simulation model to simulate the tip-sample interaction, the measurement data can be used to reveal material properties of interest which are not measured directly, such as the conductivity, sheet resistance, dielectric constant etc. of the sample under test.

In this project, the curve relating the simulated quality factor and conductivity was calibrated by a standard 200nm thick Cu thin film sample, together with the NSMM measured quality factor values of 200nm thick Ag, Au, Cr, Fe and Ti thin film samples. With this simulated curve, the experimental conductivities of the IrMn thin film samples with various doped concentrations of Al_2O_3 was found to be consistent with conventional voltammetry measurements in the same tendency. The conductivity was found to decrease as the concentration of the oxide doping increased in both measurements. Maps of the conductivity distribution on the same thin film samples were also imaged, demonstrating the ability of NSMM measure local material properties in a non-destructive manner.

In addition, the same simulation model was used to further study the effects of parameters such as tip geometry, size and tip-sample configuration on the interaction between the electromagnetic waves and the material being characterised. This study gave greater insight into the potentials and limitations of such a method of characterisation and helped to demonstrate the experimental results achieved by NSMM.

Finite element analysis (FEA) simulation implemented on the commercial software, COMSOL Multiphysics was used extensively in this study.

This project report is closely related to the following publication:

Wu, Z., de Souza, A., Peng, B., Sun, W. Q., Xu, S. Y., Ong, C. K. “Measurement of high frequency conductivity of oxide-doped anti-ferromagnetic thin film with a near-field scanning microwave microscope.” *AIP Advances* (2014) (Manuscript #2014-0263-TRR - accepted for publication in April Issue)

Table of Contents

Chapter I.....	7
Introduction.....	7
1 Historical Developments.....	8
2 Motivations	9
3 Project Objectives	10
Chapter II	12
Fundamentals	12
4 Electromagnetic Theory.....	12
5 Abbe Diffraction Limit	13
6 Near-field Theory.....	14
7 Transmission Line Theory	15
8 Lumped Series Resonant Circuit for NSMM System with Tip-Sample Interaction ...	19
9 Cavity Perturbation Theory.....	21
Chapter III.....	23
Home-designed Near-field Scanning Microwave Microscopy.....	23
10 General Working Principle	23
11 The Experimental Setup.....	24
12 The Components of the Setup.....	25
12.1 The Vector Network Analyzer (VNA) and the S11 Data	25
12.2 The Resonator and Probe Setup.....	26
12.2.1 The Quarter-wave $\lambda/4$ Coaxial Resonator and the Q Factor.....	27
12.2.2 The Probe Tip	28
12.3 Tip-sample Distance Control Equipment and Measurement Modes	29
12.4 The CCD Camera, Lens and Light Source	31
12.5 The Anti-vibration Table	31
12.6 The LabVIEW Programme	31
13 Thin Film Samples.....	32

Chapter IV.....	33
Analysis and Results	33
14 Qualitative Analysis and Results	34
14.1 S11 Response Pattern.....	34
14.2 Variation of Measured NSMM Data with Tip-sample Distance	35
15 Quantitative Analysis and Results	37
15.1 Using Finite Element Analysis as a Computational Tool.....	37
15.2 Determining the Unknown Conductivity of Al ₂ O ₃ doped IrMn Thin Film Samples.....	40
15.3 Map of Conductivity of an Al ₂ O ₃ doped IrMn Thin Film Sample	43
 Chapter V	 45
Further study with Simulations	45
16 Simulation Methodology	46
16.1 Calibration of Parameters	46
16.2 Tip-sample Configurations and Parameters.....	48
16.3 Determining Sensitivity and Spatial Resolution	50
17 Simulation Results	52
17.1 Table of Results for Various Tips on Various Thin Film Samples.....	52
17.2 Discussion on the Sensitivity and Spatial Resolution.....	55
 Chapter VI.....	 56
Conclusion and Future Work	56
 Appendix.....	 58
 References.....	 63

Chapter I

Introduction

The study of materials can be achieved by examining the interaction of electromagnetic fields with matter in the materials. In today's context, with an increased emphasis on thin film technology, nano-technology and the miniaturisation of devices, methods which allow the study of materials on a micro-scale or nano-scale are becoming increasingly valuable and important. Many of these devices are used in our everyday lives and in industries such as magnetic storage media (hard disks), liquid crystal displays, resistors, capacitors, transistors etc. Being able to determine the functionality and homogeneity of such devices and their components on a micro-scale or nano-scale are important in quality control, ensuring that the devices can operate properly.

Near-field Scanning Microwave Microscopy (NSMM) is one such tool for non-destructive characterisation of localised material electrical properties at microwave frequencies. In the near-field regime, quantitative measurement of these properties can be carried out on length scales much smaller than the freely propagating wavelength of the radiation. When a sharp probe tip protruding from the quarter-wave $\lambda/4$ coaxial resonator cavity of high quality factor Q is made to approach the sample surface with close proximity, near-field microwaves can be utilised to obtain measurements of the reflection coefficient S_{11} , quality factor Q and resonant frequency shifts of the resonant cavity coupled to the sample. Local material electrical properties such as conductivity, sheet resistance and dielectric constant etc. can then be extracted from the measured data. Of particular interest in this report is the study of the electrical conductivity of thin film samples.

1 Historical Developments

The theoretical concept of near-field microscopy was first published by Synge [1] in 1928 as a means by which to overcome the theoretical limitations of the resolving power in microscopy, potentially extending the microscopic resolution range. He proposed using an opaque screen with a sub-wavelength diameter hole (10nm diameter) held approximately 10nm above the surface of a sample which was to be passed under the aperture so that the transmitted light could be collected in a point-by-point fashion. As Synge's ideas were purely theoretical, detailed calculations of the local field distribution in the local region of the aperture and sample, which were only carried out 20 years later by Bethe [2] and Bouwkamp [3], revealed that the near fields contained a large fraction of high spatial frequency evanescent waves that result in deep sub-wavelength spatial resolution [4]. According to Novotny [5], it is no wonder that over the years, Synge's original proposals have been taken up and re-invented; unassumingly laying the groundwork for many techniques we are familiar with today, such as Scanning Electron Microscopy (SEM) and Scanning Tunnelling Microscopy (STM).

Near-field Scanning Microwave Microscopy is no exception and the use of microwaves has been explored extensively as well. In 1962, near-field microscopy using a microwave magnetic probe was performed by Soohoo [6] where the spatial variation of important magnetic properties of a sample was measured by a selective microwave resonance technique. More recently, in a paper published by Wang et al. [7] in 2005, the capability of the near-field microwave probe in quantitatively determining the sheet resistance of dissipative films was detailed. This was considered a breakthrough as the method was previously only successful in quantitatively measuring bulk materials and dielectric films. By overcoming the resolution limit as well as by proper model fitting in simulations, the quantitative measurement of dissipative thin films was achieved giving us insight into the effects of the dissipative nature of the film, the substrate used as well as the penetration depth of the method. Also, in 2009, Huang et al. [8] demonstrated the extraction of high-spatial resolution dielectric properties of bulk and thin film samples from near-field scanning at microwave frequencies. In particular, the properties were extracted from the cavity's response to the perturbation of its electromagnetic fields by the sample. Combining and comparing experimental data with Finite Element Method (FEM) calculations, the paper reports the development of an approach to more accurately model the tip-sample interaction allowing for the determination of the complex permittivity of dielectric materials at

microwave frequencies. An added analysis of the polarisation, sensitivity and spatial resolution was carried out as well.

2 Motivations

The use of near-field interactions in determining localised electrical properties of condensed matter has its advantages over more conventional far-field methods and is currently a thriving area of research. According to Anlage et al. [9], far-field methods which are carried out on the scale of the freely-propagating wavelength of radiation used (i.e. 1mm to 1m for microwave radiation) result in electrodynamic properties of samples, aggregated over macroscopic length scales [10] and do not have the capability of revealing the properties of materials that vary on much smaller length scales. Near-field methods however, allow us to study the physics of the interaction of electromagnetic waves with a material on a much smaller length scale, making up for the deficiencies of far-field methods. This is especially important today as most devices and their components have complex, multi-component features which vary on the nano-scale and require resolutions orders of magnitude smaller than the wavelength of the radiation used.

Even though a variety of near-field scanning methods may be utilised, NSMM stands out not only for its ability to non-destructively characterise the material properties of the samples at microwave frequencies, but for the relative simplicity in converting the detected signal into quantitative data such as conductivity, sheet resistance and dielectric constant etc. [11]. Another advantage NSMM has over other more mature characterisation techniques is ability to map and image the distribution of the material property of interest in the way we would use, for example, Atomic Force Microscopy (AFM) to image the topology of a sample. With the ability to map material properties, NSMM can be employed on the production line as a means by which to check on the uniformity or homogeneity of said material properties of components manufactured on a large scale. Being able to determine the quality of these components is integral to the performance of the devices that are made up of the components.

Making use of the fact that microwaves are able to penetrate materials just like X-rays, but in a less harmful way, there has been a growing interest in using NSMM to study the physics of biological systems. One such project our research group is concurrently working

on is to determine the dielectric properties of biological cells and their changes at microwave frequencies, in order to obtain novel information about cell viability and their utility; information other methods such as optical microscopy are not able to provide. The continued development of this method of characterisation is thus strongly motivated by and geared towards its potential in its future applications in the bio-medical field.

3 Project Objectives

As the experimental setup used in the CSMM laboratory is home-designed, many modifications have been made in order to improve the setup and achieve one capable of producing reliable and reproducible results. In order to study the viability and potential applications of the home-designed NSMM setup, the electrical conductivity of thin film samples will be measured.

In the NSMM measurement, the reflection parameter S_{11} , resonant frequency shift and the quality factor Q change of the resonator are obtained. However, the electrical parameters of the samples we are interested in, i.e. the conductivity of the thin film samples, cannot be measured directly. Hence in this project, we aim to build up a physical model to extract the high frequency conductivity distribution of the samples tested via NSMM measurement. In this process, the validity of the model is confirmed by simulation modelling and the modelling parameters are quantified by comparing the simulation data and measurement data of a standard Cu thin film sample of thickness 200nm, together with the NSMM measured quality factor values of Ag, Au, Cr, Fe and Ti thin film samples of the same thickness. The model can then be used to determine the unknown conductivities of oxide-doped anti-ferromagnetic thin film samples.

Finite Element Analysis (FEA) simulation using COMSOL Multiphysics will be applied as a computational tool to simulate the NSMM measurement of localised material properties and used in the extraction of the conductivity map of the thin film samples being measured. In addition, these simulations will be used to give greater insight into the potentials and limitations of such a method of characterisation. The effect of parameters such as tip-sample distance, tip size and tip material on the interaction between the electromagnetic waves and the material being characterised will be further explored to demonstrate the experimental results achieved by NSMM.

The structure of this report will be organised as follows. First, the fundamental theories governing near-field scanning techniques will be presented. Then, with a clear theoretical understanding, we move on to detail the general working principle behind the operation of NSMM and explain how our experimental setup is used to obtain the measurement data. Qualitative and quantitative analysis of the experimental and simulated results will then be carried out to give quantitative measures of the conductivities of thin film samples. Finally, the findings of the further study with simulations will be explained before the report is concluded and future directions commented on.

Chapter II

Fundamentals

This chapter illustrates several theoretical concepts closely related to near-field scanning techniques and to the workings of the NSMM setup used in our experiments. The goal of this chapter would be to connect the measurable quantities of the reflection coefficient S_{11} , quality factor Q and resonant frequency f_r to the electrical properties of the samples being probed, which are not measured directly.

4 Electromagnetic Theory

Maxwell's equations are most commonly represented as a set of partial differential equations which describe how electric and magnetic fields propagate and are affected by each other as well as by the charges and currents present [12]. There are 4 equations:

$$\nabla \cdot \mathbf{E} = \frac{1}{\epsilon_0} \rho \quad (1)$$

$$\nabla \cdot \mathbf{B} = 0 \quad (2)$$

$$\nabla \times \mathbf{E} = -\frac{\partial \mathbf{B}}{\partial t} \quad (3)$$

$$\nabla \times \mathbf{B} = \mu_0 \mathbf{J} + \mu_0 \epsilon_0 \frac{\partial \mathbf{E}}{\partial t} \quad (4)$$

where

\mathbf{E} is the electric field in V/m

\mathbf{B} is the magnetic flux density Wb/m²

\mathbf{J} is the current density in A/m²

ρ is the total charge density in C/m³

$\epsilon_0 = 8.854 \times 10^{-12} F/m$ is the permittivity of free space

$\mu_0 = 1.256 \times 10^{-6} Wb/(A \cdot m)$ is the permeability of free space

In free space, the following 2 relations also hold:

$$\mathbf{D} = \epsilon_0 \mathbf{E} \quad (5)$$

$$\mathbf{B} = \mu_0 \mathbf{H} \quad (6)$$

where

\mathbf{D} is the electric flux density in C/m²

\mathbf{H} is the magnetic field intensity in A/m

By taking the curl of Equation (3) and substituting in Equation (4), assuming there is no electric current flowing in the medium, we obtain another equation which takes the form of the differential wave equation, i.e.:

$$\nabla^2 \mathbf{E} = \mu_0 \epsilon_0 \frac{\partial^2 \mathbf{E}}{\partial t^2} \quad (7)$$

This evidences that electromagnetic fields propagate as waves in space, with an associated wavelength λ and frequency f related by the equation:

$$v = f\lambda \quad (8)$$

where v is the speed of the wave in m/s [13].

5 Abbe Diffraction Limit

The resolution of any imaging system such as NSMM has a principal maximum due to diffraction. If the imaging system can only image with a resolution corresponding to the theoretical limit of the electromagnetic radiation used, it is considered diffraction limited [14]. Let us first consider the Abbe diffraction limit on microscopy.

Abbe discovered in 1873 that light of wavelength λ , propagating in a medium with reflective index n and an angle θ , converging at point will have a diameter of:

$$d = \frac{\lambda}{2(n \sin \theta)} \quad (9)$$

The denominator of Equation (9) can reach a value of up to 4 in modern optics, giving the resolution a $\lambda/4$ Abbe diffraction limit [15]. Related to our experimental purpose, if a microwave of frequency 2.5GHz is employed in microwave microscopy, a resolution of only

3cm will be achieved, hardly comprehensive enough for the sub-wavelength study of material features. Fortunately, this diffraction limit only holds in the far-field, and as proven by Syngé and many scientists after him [16], near-field microscopy has the power to overcome the Abbe diffraction limit.

6 Near-field Theory

As briefly mentioned earlier, near-field theory has been employed in NSMM and many other scanning techniques in order to overcome the theoretical limitations of the length scale resolution of freely propagating radiation, thereby extending the microscopic resolution range. In the previous section, we have seen that for microscopy, the theoretical limit is the Abbe diffraction limit.

The near-field deals with confined electromagnetic fields which are brought in close proximity of the sample material being scanned, concentrating the fields in a small area [17]. The distance h from the source to the sample is usually in the range of $h \leq \lambda$ or $h \approx \lambda$. More specific to our experimental setup (to be detailed in Chapter III) which consists of a sub-wavelength antenna, also known as the tip, protruding from a resonant cavity, scanning in close proximity to the sample, the near-field is the portion of the radiated field closest to the tip. The tip can be considered a field concentrating feature which locally enhances probe-sample interaction [18]. Hence, the radiation distribution is largely dependent on the geometry of the tip and the properties of the surroundings, i.e. the air, sample and substrate domains [19]. The range of the near-field falls between the size of the tip, D and the wavelength λ of radiation used, i.e. $D \leq r \ll \lambda$.

Since the electromagnetic fields are localised in an arbitrary region of space, we can use the plane wave approximation [20] to first describe the freely propagating field;

$$U(\mathbf{r}, t) = A_0 e^{i(\mathbf{k}\cdot\mathbf{r} - \omega t + \varphi)} \quad (10)$$

where

A_0 is the amplitude of the wave

\mathbf{k} is the wave number given by $2\pi/\lambda$ in m^{-1}

\mathbf{r} is the arbitrary direction of the wave propagation in m

ω is the angular frequency of the wave given by $2\pi/T$ (where T is the period of the wave) in rad/s

t is a given point in time in s

φ is the phase shift of the wave in rad

In the near-field region however, we assume negligible phase difference at different points in space, i.e. $\varphi = 0$ and also since $\mathbf{k} \cdot \mathbf{r} \ll 1$, thus $e^{i\mathbf{k}\cdot\mathbf{r}} \cong 1$, the electromagnetic fields can be taken as quasi-static with a harmonic oscillating factor of $e^{i\omega t}$ [21]. This will liken the tip to an oscillating point charge source, making its interaction with the sample mainly that of capacitive coupling [22]. The electromagnetic fields in the near-field region are not transverse and decay with increasing distance from the tip as $1/r^2$ or faster, as compared to classical electromagnetic far-field radiation which falls off as $1/r$ [23]. As such, there are two contributors to the reflected signal; the far-field radiation, also known as the radiating electromagnetic field which decays as $1/r$ and the near-field radiation, also known as the evanescent field which decays as $1/r^2$ or faster.

In this way, the evanescent field which has the ability to store reactive electric energy in the tip, thus overcomes the Abbe diffraction limit and can be used in the construction of high resolution images for microscopy imaging.

7 Transmission Line Theory

The transmission line theory provides us a means to connect electromagnetic fields and circuits, thus it is of great relevance to our NSMM probe setup. In the microwave frequency range, electric and magnetic fields are responsible for power transmission and are routed from point to point by physical components of the setup. Any physical component that guides an electromagnetic wave from point to point can be considered a transmission line [24].

At low frequencies, the circuit elements are lumped since voltage and current waves affect the entire circuit at the same time. However, at microwaves frequencies, voltage and current waves do not affect the entire circuit at the same time and so the circuit must be broken down into a connection of infinitesimal unit sections, connected in series, within

which lumped circuit elements are contained [25]. This consideration has to be made because the dimensions of the circuit are comparable to the wavelength of the microwaves.

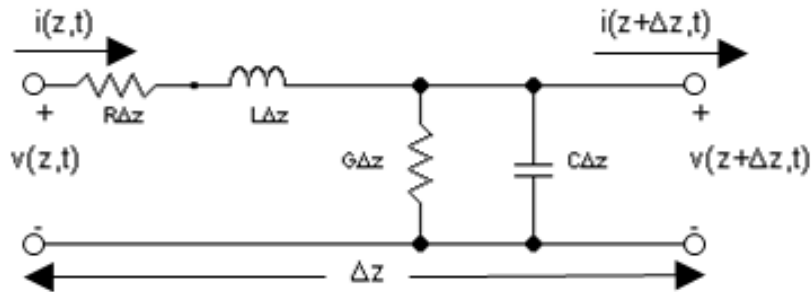


Figure 1: Illustration of a lumped circuit element section. The transmission line is the connection of infinitesimal circuit elements of this kind which consists of four lumped circuit elements, inductance L , resistance R , conductance G and capacitance C .

As shown in Figure 1 above, the circuit parameters are:

The current, $i(z, t)$

The voltage $v(z, t)$

The per unit length series resistance R

The per unit length series inductance L ,

The per unit length shunt conductance G

The per unit length shunt capacitance C

According to Kirchoff's voltage law [26],

$$v(z, t) - v(z + \Delta z, t) = R \cdot \Delta z \cdot i(z, t) - L \cdot \Delta z \cdot \frac{\partial i(z, t)}{\partial t} \quad (11)$$

According to Kirchoff's current law [27],

$$i(z, t) - i(z + \Delta z, t) = G \cdot \Delta z \cdot v(z + \Delta z, t) + C \cdot \Delta z \frac{\partial v(z + \Delta z)}{\partial t} \quad (12)$$

Considering an infinitesimal element, we divide Equation (11) and Equation (12) by Δz and take the limit $\Delta z \rightarrow 0$ and obtain:

$$\frac{\partial v(z, t)}{\partial z} = -R \cdot i(z, t) - L \frac{\partial i(z, t)}{\partial t} \quad (13)$$

$$\frac{\partial i(z, t)}{\partial z} = -G \cdot v(z, t) - C \frac{\partial v(z, t)}{\partial t} \quad (14)$$

Next, we take the steady state frequency conditions where $i(z, t) = I(z)e^{j\omega t}$ and $v(z, t) = V(z)e^{j\omega t}$ (where the imaginary number is represented by $j = \sqrt{-1}$) and arrive at:

$$\frac{\partial V(z)}{\partial z} = -(R + j\omega L)I(z) \quad (15)$$

$$\frac{\partial I(z)}{\partial z} = -(G + j\omega C)V(z) \quad (16)$$

Solving these simultaneous differential equations, we get:

$$\frac{d^2 V(z)}{dz^2} - \gamma^2 V(z) = 0 \quad (17)$$

$$\frac{d^2 I(z)}{dz^2} - \gamma^2 I(z) = 0 \quad (18)$$

where

$\gamma = \alpha + j\beta = \sqrt{(R + j\omega L)(G + j\omega C)}$ is the complex propagation constant.

Here, α is the attenuation constant and β is the real propagation constant. This means that if γ is purely real, then no propagation of electromagnetic waves occur along the transmission line.

The travelling wave solutions are thus found to be:

$$V(z) = V_0^+ e^{-\gamma z} + V_0^- e^{\gamma z} \quad (19)$$

$$I(z) = I_0^+ e^{-\gamma z} + I_0^- e^{\gamma z} \quad (20)$$

where

$e^{-\gamma z}$ represents wave propagation in positive z direction with corresponding amplitudes V_0^+ and I_0^+

$e^{\gamma z}$ represents wave propagation in negative z direction with corresponding amplitudes V_0^- and I_0^- .

Substituting Equation (19) into Equation (15) and carrying out the differentiation, we get:

$$I(z) = \frac{\gamma}{(R + j\omega L)} (V_0^+ e^{-\gamma z} + V_0^- e^{\gamma z}) \quad (21)$$

By defining $Z_0 = \frac{V_0^+}{I_0^+} = -\frac{V_0^-}{I_0^-}$, and comparing Equation (20) and Equation (21), we have the characteristic impedance of the transmission line [28]:

$$Z_0 = \frac{R + j\omega L}{\gamma} = \sqrt{\frac{R + j\omega L}{G + j\omega C}} \quad (22)$$

We can see that the transmission line is thus completely specified by its characteristic impedance Z_0 , current $I(z)$ and voltage $V(z)$.

For the purpose of NSMM, let us consider a wave incident on the interface between two media of different impedances where some of the wave gets transmitted and some reflected. With the boundary condition that overall amplitude of current and voltage must be equal in both media, we have

$$V_0^+ + V_0^- = V_1^+ + V_1^- \quad (23)$$

And correspondingly,

$$\frac{V_0^+}{Z_0} - \frac{V_0^-}{Z_0} = \frac{V_1^+}{Z_1} - \frac{V_1^-}{Z_1} \quad (24)$$

Considering the case where Medium 1 terminated in its own impedance with no further reflection after the boundary, then $V_1^- = 0$ and we solve for V_0^+ and V_0^- , we get the complex reflection and transmission coefficients [29],

$$S_{11} = \frac{V_0^-}{V_0^+} = \frac{Z_1 - Z_0}{Z_1 + Z_0} \quad (25)$$

$$S_{21} = \frac{V_1^+}{V_0^+} = \frac{2Z_1}{Z_1 + Z_0} \quad (26)$$

Of which we are particularly interested in the reflection coefficient S_{11} across the tip-sample boundary which is measured by the Vector Network Analyzer (VNA) used in our NSMM measurement.

8 Lumped Series Resonant Circuit for NSMM System with Tip-Sample Interaction

With knowledge of the transmission line model, let us now take a look at the lumped series resonant circuit for our NSMM system with tip-sample interaction.

The lumped element circuit of an electrical system is a simplifying model based on the assumption that the electrical properties of the circuit such as its resistance, capacitance and conductance etc. can be condensed into individual ideal electrical components such as inductors, resistors and capacitors etc. in a network connected by perfectly conducting wires [30].

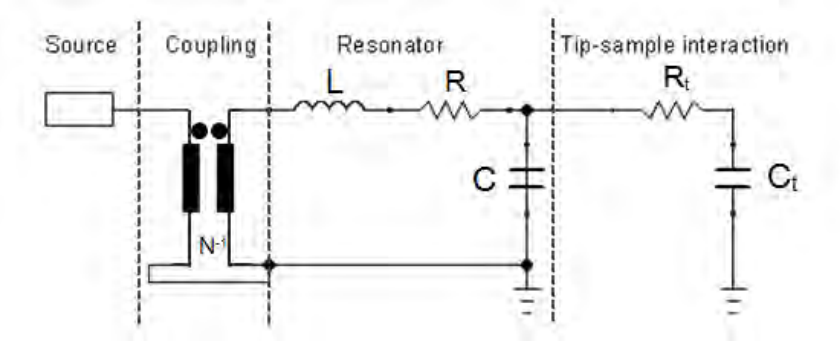


Figure 2: The lumped series resonant circuit of the NSMM setup with tip-sample interaction. Here, L , R and C represent the effective inductance, resistance and capacitance of the NSMM resonator probe setup while R_t and C_t are the lumped element resistance and capacitance of the tip-sample interaction respectively.

The lumped series resonant circuit of our NSMM system with tip-sample interaction is represented in Figure 2. For the tip in air configuration, we consider only the source, coupling and resonator with the following lumped elements; L , the effective inductance, R , the effective resistance and C , the effective capacitance. When the tip is then held above a sample during measurement, additional lumped element resistance R_t and capacitance C_t are added in parallel to the resonator's effective capacitance C . For simplicity, the tip with a resistance R_{tip} and capacitance C_{tip} and the thin film sample which is made up of a conductive layer with resistance $R_{thin\ film}$ on a less conductive substrate layer with resistance R_{sub} and capacitance C_{sub} all contribute to the lumped element resistance R_t and capacitance C_t of the tip-sample interaction depicted in Figure 2 above.

For an ideal quarter-wave $\lambda/4$ coaxial resonator in air, we can define the effective inductance L , effective resistance R and effective capacitance C by Equations (27), (28) and (29) respectively [31]:

$$L = \frac{\mu_0}{2\pi} l \ln\left(\frac{r_2}{r_1}\right) \quad (27)$$

$$R = \frac{2\sqrt{\frac{\omega\mu_0}{2\sigma}}}{\pi^3} l \left(\frac{1}{r_2} + \frac{1}{r_1}\right) \quad (28)$$

$$C = \frac{2\pi\epsilon_0}{\ln\left(\frac{r_2}{r_1}\right)} l \quad (29)$$

where

$l \approx \lambda/4$ is the effective cavity length in mm

r_1 and r_2 are the radii of the centre and outer conductors of the resonant cavity in mm

σ is the conductivity of the metal, i.e. copper has a value of $\sigma = 5.88 \times 10^7 S/m$

μ_0 and ϵ_0 are the permeability and permittivity of free space respectively

More specific to our NSMM setup, the resonant cavity and centre conductor are fabricated with copper and the specific dimensions are given by $l = 21mm$, $r_1 = 0.8mm$, $r_2 = 4mm$. These dimensions yield an inductance $L = 6.75nH$, a resistance $R = 2.96\Omega$ and a capacitance $C = 0.716pF$.

In addition, the resonant frequency f_r and quality factor Q of the resonant cavity are related to the total inductance L' , total resistance R' and total capacitance C' by the following equations [32],

$$2\pi f_r = 1/\sqrt{L'C'} \quad (30)$$

$$Q = \frac{1}{2\pi f_r C' R'} \quad (31)$$

Thus we can see that during NSMM measurements, the tip-sample interaction which is represented by the additional lumped elements of resistance R_t and capacitance C_t in Figure 2 behave like an additional impedance Z_t to the original lumped series resonant circuit (comprising only the source, coupling and resonator). In general, Z_t depends on tip geometry, sample properties and the tip-sample distance [33]. This in turn will result in the deviation of the measured resonant frequencies and quality factors from their tip in air values.

By employing the cavity perturbation theory, to be discussed in the following section, the quantifiable deviation of the measured values mentioned above can then be used in the extraction of other electrical properties of the samples being probed.

9 Cavity Perturbation Theory

Let us first take a look at the general theory behind the cavity perturbation approach. When a resonant cavity is perturbed by the introduction of a sample, with distinct material properties, within close proximity of the cavity, the electromagnetic fields inside the cavity are changed and differ slightly from the electromagnetic fields before the change [34]. The corresponding changes in resonant frequency f_r and quality factor Q , associated with the measurements taken in air and over different samples, can then be related to other electrical parameters.

In his work, Anlage [35] briefly explored the idea of using the cavity perturbation approach in the measurement of a low-loss homogeneous dielectric thin film sample of unknown complex permittivity, $\epsilon_{film} = \epsilon'_{film}(1 - i \tan \delta)$.

In his example, the cavity perturbation theory showed that:

$$\frac{\Delta f_r}{f_r} \cong -(\epsilon'_{film} - 1) \frac{\epsilon_0}{4W} \int_{V_t} E_1 \cdot E_2 dV \quad (32)$$

$$\Delta\left(\frac{1}{Q}\right) = -\tan \delta \frac{2\epsilon'_{film}}{\epsilon'_{film} - 1} \frac{\Delta f_r}{f_r} \quad (33)$$

where

W is the total energy stored in the resonator

V_t is the volume of the thin film

E_1 and E_2 represent the original and perturbed electric fields respectively

ϵ_0 is the permittivity of free space

The aim would then be to determine the values of ϵ'_{film} and $\tan \delta$ so as to quantify ϵ_{film} , the complex permittivity of the homogeneous thin film sample from the measureable experimental data of $\frac{\Delta f_r}{f_r}$ and $\Delta\left(\frac{1}{Q}\right)$ on the LHS of the Equations (32) and (33) respectively.

On the RHS of Equation (32), the electric fields E_1 and E_2 can be taken as the solutions to Poisson's equation, under the electrostatic approximation, which is valid for distances much smaller than the wavelength of electromagnetic radiation emitted from the source, as in this case. The integration over the thin film volume V_t can be carried out using Finite Element Analysis (FEA) simulations on COMSOL Multiphysics software (to be elaborated on in Chapter IV Section 15.1). The total energy stored in the resonator, W is an unknown constant which can be found from calibration of known samples using the same simulations. Once ϵ'_{film} is found, we can substitute it into Equation (33) to obtain $\tan \delta$ so that the complex permittivity of the homogeneous thin film sample ϵ_{film} can be quantitatively determined.

Likewise, in this report we will make use of the cavity perturbation approach to extract the conductivity of thin film samples from the same measurable experimental data. Together with this approach and knowledge of the aforementioned theoretical concepts which govern the use of NSMM as a method of characterisation, we move on to the description and use of our home-designed near-field scanning microwave microscopy setup.

Chapter III

Home-designed Near-field Scanning Microwave Microscopy

This chapter will serve to explain the general working principle of NSMM as well as to introduce the experimental setup and components used in the measurement of thin film samples.

10 General Working Principle

For our NSMM methodology, the general principles of electromagnetic resonance perturbation can be applied. The quarter-wave $\lambda / 4$ coaxial resonator and probe setup connected to the VNA works as a detection system and its electromagnetic response is monitored as the tip takes measurements over the sample in a point by point manner. The variation of electrical properties of the sample will perturb the electric interaction between the tip and the sample, to an extent where even minute changes can cause significant perturbations to the tip-sample interaction. The tip-sample interaction can then be likened to an electric or magnetic field penetrating the sample, with the size of the penetrating field closely related to the tip size D due to the quasi-static nature of the near-field [36]. This means that the signal acquired is taken from a small part, approximately the tip size D , of the sample at any one time, giving us localised measurements.

Because the electromagnetic response of the near-field microwave probe can be attributed to the ability of evanescent fields to store reactive electric energy in the tip, the perturbations then cause a change in the energy stored, which in turn affects the electromagnetic response of the near-field microwave probe [37]. These changes are then reflected as changes in S_{11} amplitude, a resonant frequency shift as well a change in the quality factor Q , allowing us to then quantitatively derive the electrical properties of the sample. In this report, we will focus on measurement of the conductivity of thin film samples.

11 The Experimental Setup

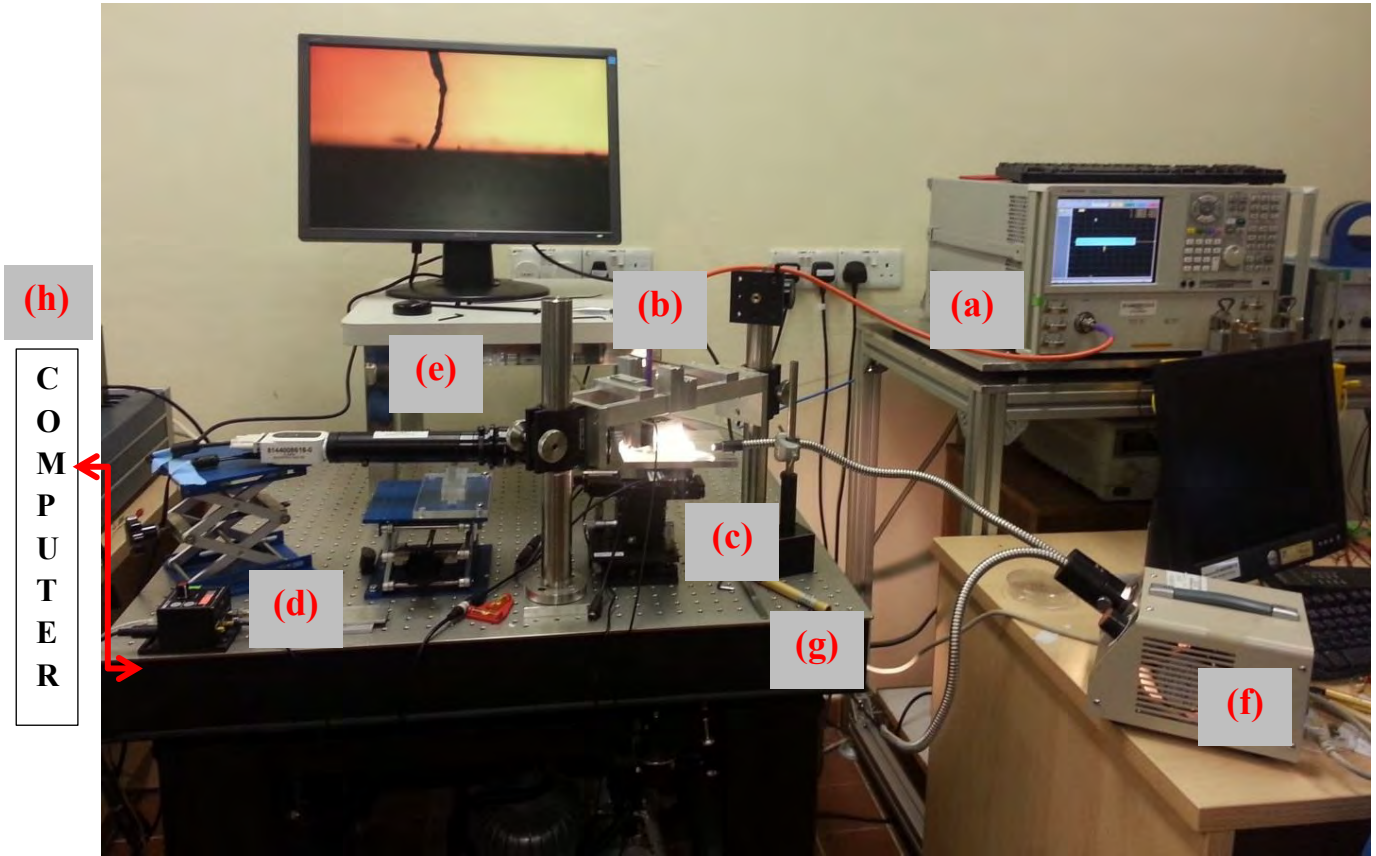


Figure 3: The home-designed NSMM setup developed in the CSMM lab made up of various components; (a) Vector Network Analyzer (VNA), (b) Quarter-wave coaxial resonator and probe setup, (c) xy precision tuner stage, (d) z piezoelectric motor, (e) CCD camera and lens, (f) Light source for CCD monitoring (g) Anti-vibration table (h) Computer for programming and controlling the measurement (out of view of picture).

The research team in the CSMM lab has made many modifications to the development of the NSMM system before arriving at the current setup shown in Figure 3 above.

Taking a closer look, the Vector Network Analyzer (VNA) (Agilent Technologies N5230A) (a) is connected by a high quality thick coaxial cable (bandwidth 0-50GHz) to the quarter-wave $\lambda/4$ coaxial resonator and probe setup. The quarter-wave $\lambda/4$ coaxial resonator and probe setup (b) is placed in the resonator basket which allows us to keep the probe at an adjustable height above the xy precision tuner stage and motor. The xy precision tuner stage (Zaber T-LS28E-KT03) (c) holds the various thin film samples to be measured. During measurement, the vertical displacement of the probe is finely controlled by the z piezoelectric motor (Thorlab TPZ001) (d). The CCD camera and lens (e) are the most recent additions to the setup and have been found to be extremely useful in providing us a means to visually monitor the tip-sample region, with the aid of the light source (f), used to illuminate the tip-

sample region. The measuring components of the setup are secured onto the anti-vibration table (g). Lastly, a computer (h) is connected to the setup on which we use a programme, LabVIEW to control the system as well as to collect data from the VNA.

12 The Components of the Setup

12.1 The Vector Network Analyzer (VNA) and the S11 Data

The vector network analyzer (VNA) is an instrument that measures the amplitude and phase properties of the transmission and reflection of electrical networks at high frequencies. A signal generator generates microwaves at various frequencies within a specified range. The signal generator output is then routed to the quarter-wave $\lambda/4$ coaxial resonator and probe setup and the signal to be measured is subsequently routed back to the receiver on the VNA. The receiver then makes measurements of the amplitude, frequency and phase of the reflection signal, S11.

There are two wave ports on the VNA, of which we only make use of the reflection signal, S11 port which is to be calibrated before any measurement is taken. From the transmission line theory (detailed in Chapter II Section 7); we found that the reflected wave from an interface between two propagation media of different wave impedance is given by:

$$S_{11} = \frac{V_{0-}}{V_{0+}} = \frac{Z_1 - Z_0}{Z_1 + Z_0} \quad (34)$$

Using the calibration kit, the open port load ($Z = \infty$), short port load ($Z = 0\Omega$) and broadband load ($Z = 50\Omega$) can be applied at the end of the high quality thick coaxial cable so that the VNA receiver can correct for any contribution to the overall wave impedance of the cable at various frequency values.

Once calibration is complete, measurement can be carried out. The VNA display shows us the change in the amplitude of the reflection signal S11, resonant frequency shifts as well as the change in quality factor Q , as shown in Figures 4(a) and (b) on the next page.

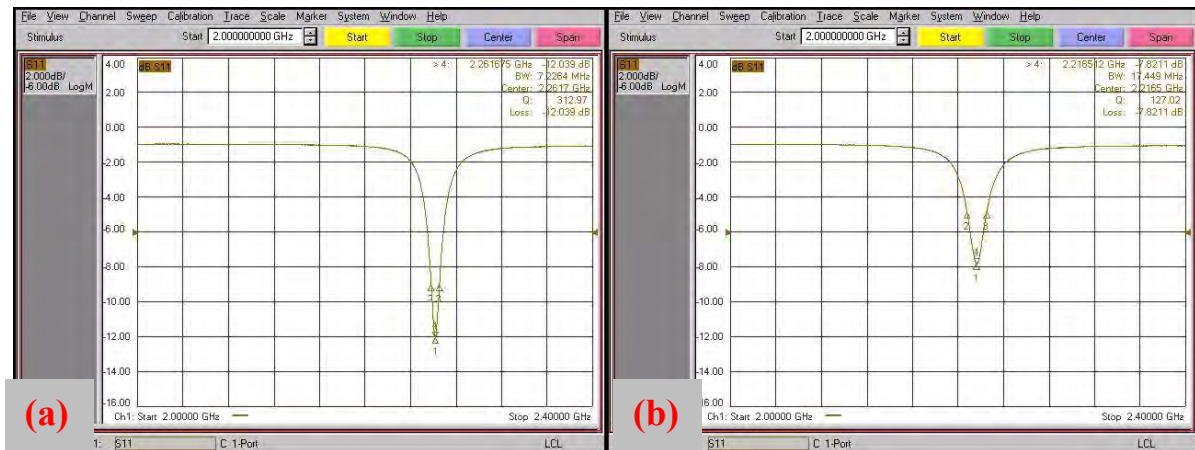


Figure 4(a) and 4(b): Both images are of the displays on the VNA which show the amplitude of the S11 signal and gives us quantitative values of the resonant frequency, magnitude of the S11 signal, bandwidth and quality factor (Q) corresponding to the respective tip-sample geometries (as shown in the top right hand corner). Fig. 4(a) corresponds to a metallic tip in air, while Fig. 4(b) corresponds to a metallic tip over a Silicon substrate. There is a shift in resonant frequency to the left as well as a decrease in S11 amplitude in Fig. 4(b) as compared with Fig. 4(a).

12.2 The Resonator and Probe Setup

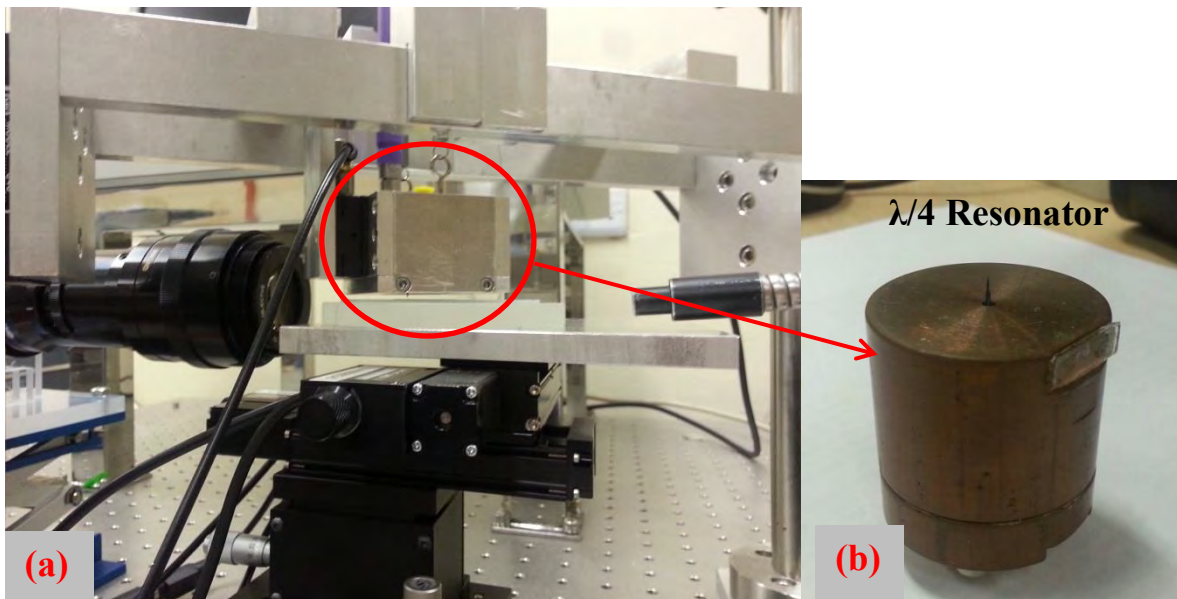


Figure 5(a): Zoomed-in view of the quarter-wave $\lambda/4$ coaxial resonator and probe setup held in the resonator basket over the xy precision tuner stage on which thin film samples are placed for measurement. Figure 5(b): The quarter-wave resonator with metallic probe tip mounted on the center conductor of the resonator.

After the quarter-wave $\lambda/4$ coaxial resonator is prepared, connections cleaned and tested for conductivity, the chosen tip is mounted on the center conductor as shown in Figure 5(b). The resonator is then turned upside down and carefully inserted into the resonator basket so that the tip protrudes downwards over the samples placed on the xy precision tuner stage for measurement.

12.2.1 The Quarter-wave $\lambda/4$ Coaxial Resonator and the Q Factor

Each quarter-wave $\lambda/4$ coaxial resonator consists of an outer cylindrical shield and base shield, two coupling coils as well as a shorted centre conductor of coaxial cable, with a length exactly $\lambda/4$ at the prescribed resonant frequency f_r . The reason for using such a resonator is to take advantage of the high quality factor Q . The quality factor Q of the quarter-wave $\lambda/4$ coaxial resonator is found by taking the ratio of the centre frequency f_r to the 3dB power bandwidth Δf , thus characterising the resonator's bandwidth relative to the centre frequency. In Figure 4(a) and 4(b) (found on the previous page), the 3dB bandwidth is indicated by the triangular markers 2 and 3. Here, we can see that a smaller bandwidth, thus sharper peak, results in a higher quality factor Q while a larger bandwidth, thus broader peak, results in a lower quality factor Q . For the resonators used in the experimental setup, the highest quality factor Q attained was over 2000 at a resonant frequency of 2.3GHz.

In physical terms, the quality factor Q can be defined as the ratio of the energy stored in the resonator to the energy dissipated per cycle per unit time:

$$\begin{aligned} Q &= 2\pi f_r \frac{\textit{Energy stored}}{\textit{Energy dissipated per cycle per unit time}} \\ &= 2\pi f_r \frac{E_{total}}{P_{loss}} \end{aligned} \quad (35)$$

where

f_r is the resonant frequency

E_{total} is the average energy stored in the cavity

P_{loss} is the energy loss per second

12.2.2 The Probe Tip

Copper, Tungsten and Carbon Nano-tube (CNT) bundled tips were prepared in the CSMM lab for use in the experimental setup. Before conducting each set of experiments, we can choose the tip to be used and the selected tip can be easily mounted on the resonator.

The metallic tips, i.e. Copper and Tungsten were fabricated by anode corrosion with 1M NaOH and the average radii of the tips fabricated are around $5\mu\text{m}$ to $10\mu\text{m}$. For the measurement and scanning of the thin film samples, the Copper tips were used. In Figure 6(a) and (b), we have the Scanning Electron Microscopy (SEM) images of the apex of the same Copper tip used in our NSMM measurement. From the images, we can see that the tip has been fabricated to have a tapered end with a diameter around $14\mu\text{m}$. By choosing a tapered end as such, the electromagnetic field can emanate from the tip apex as a point source, thus can be used for localised measurements.

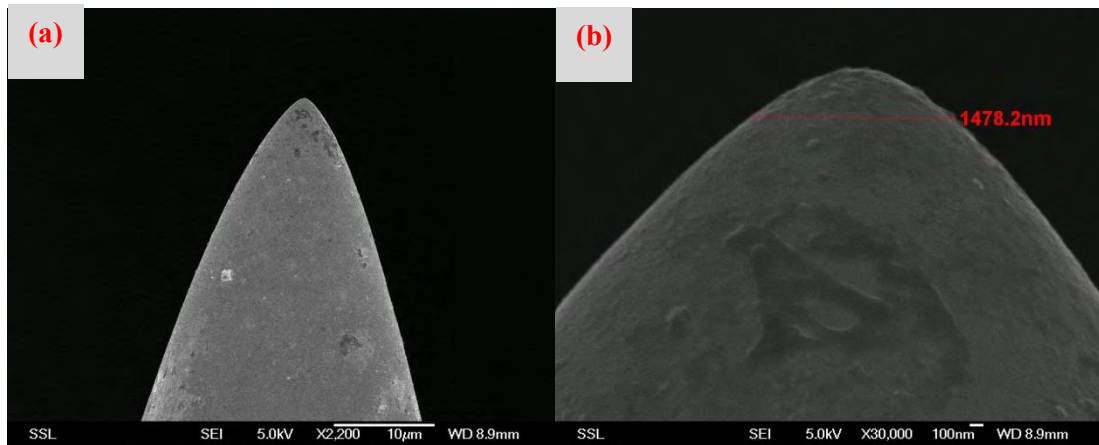


Figure 6 (a) and (b): SEM images of the Copper tip used in our NSMM measurement. Figure 6(b) is the zoomed in image of the apex of the same tip in figure (a) with the diameter of the tapered end indicated as 1478.2nm (approximately $14\mu\text{m}$).

As for the CNT bundled tips, they were prepared by attaching a CNT bundle onto the pre-prepared metallic tips with the use of highly conductive silver paste as glue. As the CNT bundle itself is highly conductive, an additional layer of non-conductive glue was coated onto the bundle. This allows us to engage the CNT bundled tip in contact mode or in tapping mode (to be detailed in Section 12.3) without having to worry about causing instability to the measurement due to the contact between the conductive tip and sample. In addition, the coating also helps to maintain the shape of the bundle during measurement. This is important as the bundle is made up of hundreds of carbon nanotubes which on contact can loosen and spread out. An analogy to the CNT bundle would be a household broom used to sweep floors which spreads out considerably when in contact with the floor. The spreading of the CNT

bundle will greatly reduce the resolution of the measurements or images obtained and thus is undesirable.

As mentioned earlier on in the report, the geometry of the tip and tip size play an important role in determining the radiation distribution of the microwaves as well as the corresponding impedance contribution from the tip-sample interaction. Thus, it is meaningful to study the effect of different tip properties on the sensitivity and spatial resolution of the measured data. Because the precise size and shape of the tips were difficult to control in the fabrication process, instead of physically experimenting with various tips, simulations were conducted for the study of the effect of tip properties and the findings will be detailed in Chapter V.

12.3 Tip-sample Distance Control Equipment and Measurement Modes

Before measurement commences, the thin film samples are carefully placed on the xy precision tuner stage where the corresponding xy displacement of the stage with respect to the probe can be manually adjusted and centred. The height of the stage is also adjusted so that it approaches the probe tip at the optimum tip-sample distance. During measurement, LabVIEW software is used to automatically control the precise step motion of the stage in the x and y directions, with a lateral motion resolution as fine as $0.047625\mu\text{m}$ per step (as specified by the manufacturers), for area mapping and scanning of the samples. In reality, the average step size achievable with the open looped controller can be taken as $0.05\mu\text{m}$ with any deviation from this value considered negligible. The average time taken for each point measurement is around 10ms and the time taken for the xy precision tuner stage to move between spots is about 100ms.

To control the z displacement of the tip over the sample, we employ the use of a TPZ001 piezoelectric motor which allows for manual or automated nanometer level motion control. Its high voltage output range of 75V corresponds to a distance control range of 0 to $25\mu\text{m}$ with a resolution of 0.33nm/mV . The piezoelectric motor is used like a feedback control system which maintains the tip's up-down motion with respect to the sample via a connection to the resonator basket. Hence, tip-sample distance can be maintained at a constant during measurement and scanning.

The tip can be engaged in one of three different measurement/ scanning modes:

Contact mode: The tip scans the sample in close contact with the surface. As the tip is in contact with the samples being scanned, high resolutions can be achieved however; the tip and the sample may be damaged in this mode and can distort measurements.

Soft-contact mode: The tip hovers a few nanometers above the sample surface. This allows for good tip-sample interaction without causing damage to the tip or to the samples being measured.

Tapping mode: As the name suggests, the tip is alternately placed in contact with the surface and then subsequently lifted off the surface to avoid dragging the tip across the surface and the tapping motion is controlled by the piezoelectric motor. This allows for high resolution imaging without causing damage to the samples being measured.

For our measurement of the thin film samples, the tips used were mainly copper tips with good conductance. As a result, soft contact between the tip and sample made the measurements unstable. In order to overcome this, a variation of soft-contact mode was used where tip-sample distances were maintained at 100nm for quantitative measurement and 1µm for scanning and imaging. Even at such tip-sample distances, the tip-sample interaction was good enough for us to obtain conclusive results.

12.4 The CCD Camera, Lens and Light Source

The CCD camera and lens were used as a visual aid in ensuring that the probe is engaged in the appropriate measurement mode. The display on the monitor in Figure 3 (on pg. 24) shows distinctly a CNT bundled tip in contact with the sample. The measurement was carried out in tapping mode.

12.5 The Anti-vibration Table

As the measurement system is highly sensitive and involves tip-sample distances of only a few hundred nanometers, it is important that any background mechanical vibration due to other components of the setup, such as the VNA and the computer, are minimised. To eliminate any noise in the readings due to vibrations from external sources, the measuring system of the setup was secured onto the anti-vibration table.

12.6 The LabVIEW Programme

The VNA, the xyz precision tuner stage and the z piezoelectric motor are all connected to a computer on which we use a LabVIEW programme. The LabVIEW programme thus allows for automated stage control, piezoelectric motor control as well as automated data acquisition from the VNA.

13 Thin Film Samples

In our experiments, metallic thin film samples as well as oxide doped anti-ferromagnetic thin film samples were used.

The metallic thin film samples were prepared in the CSMM lab by sputtering the desired metal onto Silicon or Silicon dioxide substrates. Metals such as Silver, Aluminium, Gold, Cobalt, Chromium, Copper, Iron and Titanium were deposited on substrates. The thickness of each film was 200nm. These metallic thin films were homogeneous thin films and so the electrical properties at one point of the thin film should not differ significantly from the electrical properties at an adjacent point on the film.

The oxide doped anti-ferromagnetic thin film samples, i.e. Al_2O_3 doped IrMn thin films were also prepared in the CSMM lab by RF sputtering onto Silicon dioxide substrates. The doping concentration was adjusted by varying the number of Al_2O_3 chips attached onto the IrMn target. The thickness of each film was also 200nm.

In our experimental procedure, we first carried out measurements on the metallic thin films of known electrical conductivity in order to calibrate our NSMM measurements before proceeding to measure the Al_2O_3 doped IrMn thin film samples of unknown conductivity. The results and analysis of our experiments will be elaborated in the next chapter.

Chapter IV

Analysis and Results

In this chapter, we will look at how the unknown conductivity of oxide doped anti-ferromagnetic films as well as a mapping of the high frequency conductivity distribution of these films can be derived from the quality factor Q data of the NSMM measurements.

Metallic thin film samples of known conductivity as well as the Al_2O_3 doped IrMn thin film samples of unknown conductivity were measured using the experimental setup detailed in the previous chapter. The corresponding calculations then entailed the use of Finite Element Analysis (FEA) simulations on COMSOL Multiphysics to simulate the tip-sample interaction, allowing us to analyse the relationship between the change in quality factor Q and conductivity. By using a standard Copper thin film sample, a simulated reference curve of quality factor Q VS conductivity was obtained so that the unknown conductivity of the Al_2O_3 doped IrMn thin film samples could then be quantified. This allowed us to investigate the effect of oxide doping on the anti-ferromagnetic films being tested.

14 Qualitative Analysis and Results

14.1 S11 Response Pattern

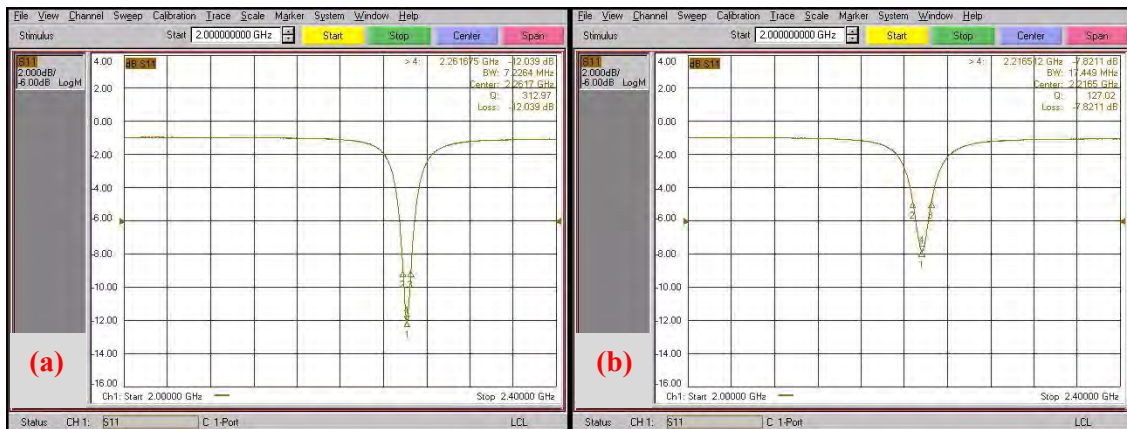


Figure 7(a) and 7(b): Both images are of the displays on the VNA which show the amplitude of the S11 signal and gives us quantitative values of the resonant frequency, magnitude of the S11 signal, bandwidth and Quality factor (Q) corresponding to the respective tip-sample geometries (as shown in the top right hand corner). Fig. 7(a) corresponds to a metallic tip in air, while Fig. 7(b) corresponds to a metallic tip over a Silicon substrate. There is a shift in resonant frequency to the left as well as a decrease in S11 amplitude in Fig. 7(b) as compared with Fig. 7(a).

Shown in Figure 7(a) and 7(b) are images of the displays on the VNA for a tip in air configuration as well as a tip over sample configuration respectively. In Fig. 7(b), we see that there is a significant decrease in the S11 amplitude, a broader bandwidth as well as a shift of the S11 signal peak towards a lower frequency value as compared to Fig. 7(a). These changes can be attributed to the change in the coupling between the tip and sample.

When the probe tip comes into contact with the metallic thin film samples, the S11 peak from VNA will become unstable and disappear such that the magnitude of S11 approaches 0. Hence, it is important that by observing from the monitor, the tip is adjusted so that it approaches the thin film sample surface with a tip-sample distance maintained at several hundred nanometers or microns. The LabVIEW programme which controls the piezoelectric voltage can then be increased gradually and subsequently stopped when the magnitude of S11 reached a value higher than -3dB. In this way, the tip-sample distance of 100nm for measurement and 1 μ m for imaging can be realized.

14.2 Variation of Measured NSMM Data with Tip-sample Distance

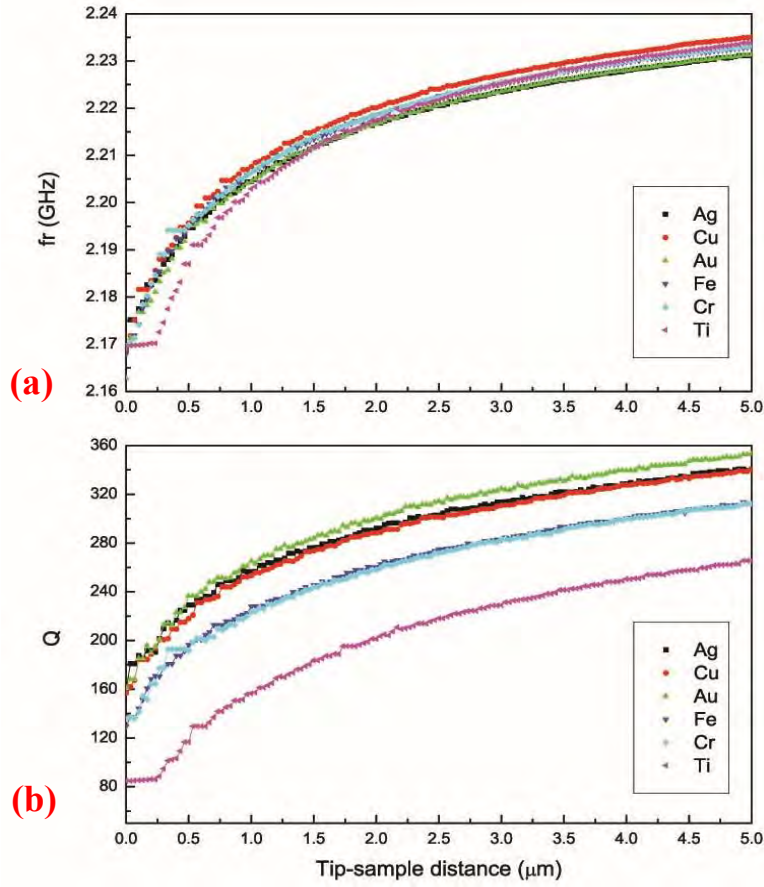


Figure 8(a): A plot of the measured resonant frequency f_r over a range of tip-sample distances for various metallic thin film samples.

Figure 8(b): A plots of the measured quality factor Q over a range of tip-sample distances for various metallic film samples.

In Figure 8(a), we see the variation of the measured resonant frequency f_r with tip-sample distance while in Figure 8(b), we see the variation of the measured quality factor Q also with tip-sample distance for various metallic films samples prepared on SiO_2 substrates. Both plots show an increasing trend where the resonant frequency f_r and the quality factor Q increase with tip-sample distance.

Focusing first on the resonant frequency plot of Figure 8(a), we recall the lumped series resonant circuit of our NSMM system (on pg. 19). In the lumped series resonant circuit, an increase in tip-sample distance decreases the tip-sample coupling capacitance C_t , thus resulting in an overall decrease of the total capacitance C' . From Equation (30),

$$2\pi f_r = 1/\sqrt{LC'} \quad (30)$$

we know that resonant frequency f_r is inversely proportional to the square root of the product of the inductance and capacitance. This explains why an increase in tip-sample distance (which corresponds to a decrease in total capacitance C') will cause a corresponding increase in the resonant frequency f_r as shown by the trend in Figure 8(a).

For metallic thin film samples, the tip-sample capacitance C_t is largely determined by the tip-sample coupling and the capacitance of the dielectric SiO_2 substrate instead of the capacitance of the various metallic layers deposited on each SiO_2 substrate. This is because the thin films deposited are typically only few hundred nanometres thick (i.e. 200nm thick in our case) and so it brings about only a very small change in the frequency shift as compared with the effect of the bulk substrate. As a result, we see much overlap and little variation in the plots of the resonant frequency across the different metallic film samples in Figure 8(a).

Next, we consider the quality factor Q plot of Figure 8(b). Recalling Equation (35),

$$\begin{aligned} Q &= 2\pi f_r \frac{\textit{Energy stored}}{\textit{Energy dissipated per cycle per unit time}} \\ &= 2\pi f_r \frac{E_{total}}{P_{loss}} \end{aligned} \quad (35)$$

we see that the quality factor Q is mainly determined by the average energy stored in the cavity as well as energy loss per unit time. Because the energy losses over the metallic thin film samples are unique to each metal deposited on the SiO_2 substrates, the corresponding change in quality factor Q is more sensitive as compared to the change in resonant frequency f_r measured across the range of tip-sample distances. This is evident in Figure 8(b) where the plot for each metallic thin film can be distinguished from each other. Using the cavity perturbation theory (detailed in Chapter III Section 9), we found that the introduction of the sample in the region close to the tip can be treated as a perturbation. With an increase in tip-sample distance, the quality factor Q also increases as there is less energy loss from the perturbation by the sample.

As is consistent with the study conducted by Wang et Al. [7], we find that resonant frequency is rather insensitive to conductivity changes, thus for a thin film layer that is more conductive than the substrate layer, only changes in the measured quality factor Q corresponding to the different conductivities of the thin film samples are needed in the determination of the unknown conductivity of the Al_2O_3 doped IrMn thin film samples in the rest of our analysis.

15 Quantitative Analysis and Results

15.1 Using Finite Element Analysis as a Computational Tool

Finite Element Analysis (FEA) simulations were performed on COMSOL Multiphysics to simulate the interaction between the tip and the samples being probed. Using the RF module, which can characterise electromagnetic fields for microwave devices, a 2D axial symmetric model of the tip-sample configuration was drawn. By defining the relevant boundaries and domains, our model was created to resemble the actual experimental configuration as closely as possible.

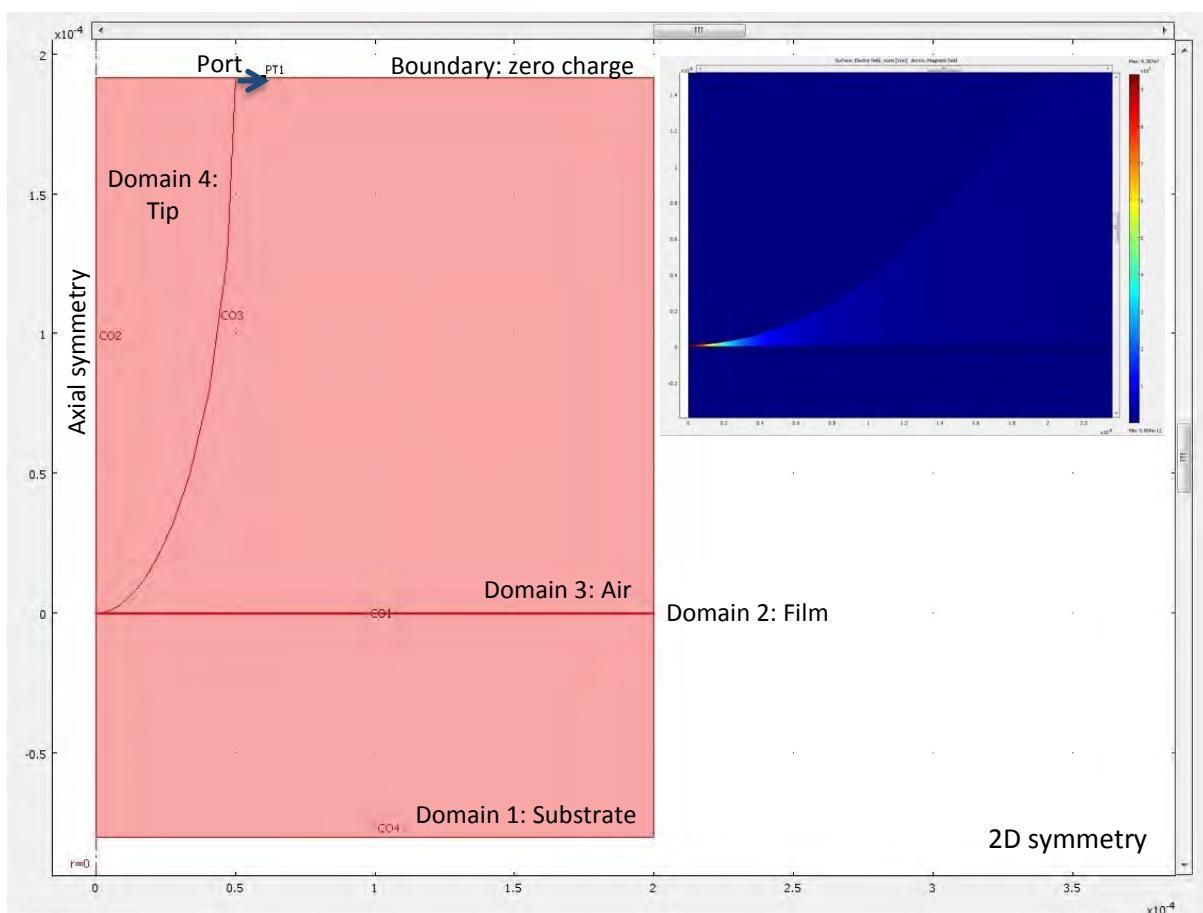


Figure 9: An example of the axial symmetric model of the tip-sample geometry, modelled on the RF module of COMSOL Multiphysics for FEA calculations. In this model we see a tip (sphere-capped and of $5\mu\text{m}$ radius) positioned above a 200nm thin-film layer on a Silicon substrate (with a tip-sample distance of 100nm). The inset shows the variation of the electric field, which is concentrated beneath the tip.

In Figure 9 above, we illustrate an example of the modelled tip-sample geometry. It features a $5\mu\text{m}$ radius, sphere-capped Copper tip over a 200nm thin film sample prepared on a Silicon substrate with a tip-sample distance of 100nm . Electromagnetic waves with a frequency of 2.2GHz and 1W power are excited into the tip-sample geometry via the coaxial

port (indicated by the blue arrow). As FEA calculations are to be carried out, the finite element mesh used is especially fine, composing of over 360000 elements.

Once the finite element model is meshed and solved, post-processing allows us to extract specific simulated data related to the experimental quality factor data. Other data can also be calculated and visually represented. For example, in the inset of Figure 9, found by solving Poisson's equations (computed in the simulations) is the near-field electric field distribution. We can see that a strong electric field is concentrated in the region between the apex of the tip and the sample, which is why localised measurements are obtained in NSMM.

As mentioned briefly in the previous section, the dependence of the quality factor Q on the energy loss per second (power loss) results in its distinct changes. Hence, it is worthwhile to expand Equation (35) further:

$$\begin{aligned}
 Q &= 2\pi f_r \frac{\text{Energy stored}}{\text{Energy dissipated per cycle per unit time}} \\
 &= 2\pi f_r \frac{E_{total}}{P_{loss}} = 2\pi f_r \frac{E_{total}}{P_{cavloss} + P_{tip\ loss} + P_{resis.\ heat}} \quad (35a)
 \end{aligned}$$

where

$P_{cavloss}$, the power loss in the resonant cavity walls,

$P_{tip\ loss}$, the power loss in the form of radiation due to tip-sample interaction

$P_{resis.\ heat}$, the power loss due to the resistive heating of the thin films

In our NSMM measurements, the total energy stored in the resonant cavity E_{total} and the power loss in the resonant cavity walls $P_{cavloss}$ can be assumed as constant because the same resonator is used throughout. These parameters are independent of sample properties.

For the tip in air configuration and the tip over sample configuration, Equation (35a) can be represented as:

$$Q_{air} = 2\pi f_r (air) \frac{E_{total}}{P_{cavloss} + P_{tip-air\ loss}} \quad (36)$$

and

$$Q_{sample} = 2\pi f_r (sample) \frac{E_{total}}{P_{cavloss} + P_{tip-sample loss} + P_{resis. heat over sample}} \quad (37)$$

respectively. From here, it is clear that the change in quality factor Q_{sample} can be attributed mainly to the unique power loss due to resistive heating $P_{resis. heat over sample}$ on the various metallic thin film samples as compared to the tip in air quality factor Q_{air} .

In our simulations, $P_{tip loss}$ can be quantified by the integration along the tip boundary while $P_{resis. heat}$ is quantified by the integration over all domains of the tip-sample geometry in Figure 9 (on pg. 37) respectively. In this way, for a standard 200nm Copper thin film sample deposited on SiO_2 substrate of conductivity $\sigma = 5.88 \times 10^7 S/m$, the unique values of $P_{tip-sample loss}$ and $P_{resis. heat over sample}$ can be quantified. By putting this simulated data together with the experimentally obtained data of Q_{air} , $f_r (air)$, Q_{Cu} and $f_r (Cu)$ in Equations (36) and (37), the constants E_{total} and $P_{cavloss}$, can then be found as well. Here, E_{total} was found to be $6.24 \times 10^{-16} J$ and $P_{cavloss}$ was found to be $3.86 \times 10^{-8} W$.

Having calibrated the constants E_{total} and $P_{cavloss}$ (associated with the resonator used), the curve of the simulated quality factor Q can be plotted against a range of conductivities σ .

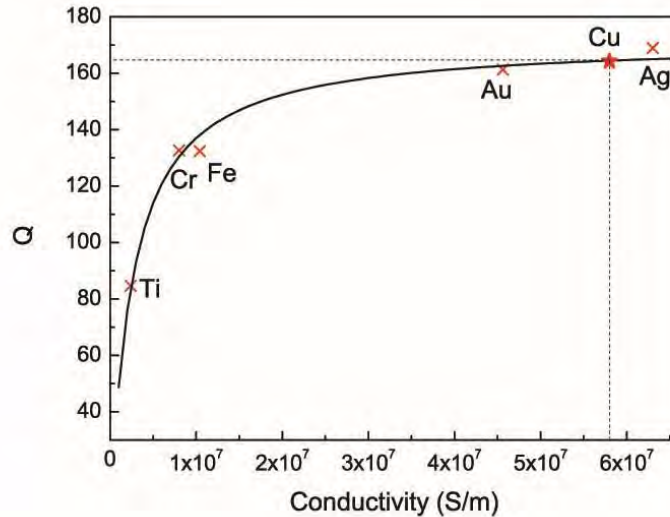


Figure 10: The simulated quality factor plotted against a range of conductivities as calibrated by a standard Cu thin film sample. In the figure, the red star represents the measured quality factor of 164.2 corresponding to the Cu thin film sample with a conductivity of $5.88 \times 10^7 S/m$ and this value is used as a reference for the rest of the curve. The experimentally determined Q factor of Ti, Cr, Fe, Au and Ag thin film samples are marked with the red crosses and are found to be consistent with the simulated data.

In Figure 10, we have the simulated curve of the quality factor plotted against a range of conductivities as calibrated by a standard Cu thin film sample. In the figure, the red star represents the measured quality factor of 164.2 corresponding to the Cu thin film sample with a conductivity of $5.88 \times 10^7 S/m$ and this value is used as a reference for the rest of the curve. The experimentally determined Q factors of Ti ($\sigma = 2.38 \times 10^6 S/m$, $Q = 84.7$), Cr ($\sigma = 8.00 \times 10^6 S/m$, $Q = 132.6$), Fe ($\sigma = 1.04 \times 10^7 S/m$, $Q = 132.4$), Au ($\sigma = 4.56 \times 10^7 S/m$, $Q = 161.0$) and Ag Ti ($\sigma = 6.30 \times 10^7 S/m$, $Q = 169.0$) thin film samples are marked with the red crosses.

Though there were very few experimental points taken due to the availability of the metallic thin film samples, it can be seen that the experimental data plotted above are found to be consistent with the simulated curve, thus the consistency allows us to apply the $Q - \sigma$ curve in the quantitative derivation of the unknown conductivity of the Al_2O_3 doped IrMn thin film samples.

15.2 Determining the Unknown Conductivity of Al_2O_3 doped IrMn Thin Film Samples

In the same procedure used to acquire NSMM measurements of the resonant frequency f_r and the quality factor Q of the metallic thin film samples, NSMM measurement of the Al_2O_3 doped IrMn thin film samples was also carried out.

Consistent with the resonant frequency shifts of metallic thin films, little change in the resonant frequencies was observed across the Al_2O_3 doped IrMn thin film samples and the resonant frequencies obtained were all around 2.17GHz. The quality factors showed distinct changes for the different compositions of the Al_2O_3 doped IrMn thin film samples, thus will be used for further analysis.

The Al_2O_3 doped IrMn thin film samples were also measured with Energy Dispersive X-ray Spectroscopy (EDS) (Hitachi S4800 SEM) so that the atom content of Aluminium in each of the Al_2O_3 doped IrMn thin film samples could be determined. The atom content of Aluminium in the Al_2O_3 doped IrMn thin film samples was found to range between 0.88% and 13.79%.

With this information, the experimentally obtained quality factors from NSMM measurement can then be plotted against the atom content of Aluminium as shown in Figure 11(a) on the next page. In the figure we see five measurements made on each of the Al_2O_3 doped IrMn thin film samples with different doping concentration. The quality factor Q corresponding to each sample showed an overall decreasing trend, thus the higher the atom content of Aluminium the lower the measured quality factor. This means that the higher the doping concentration of Al_2O_3 in each sample, the lower the quality factor Q measured.

Using the simulated conductivity curve in Figure 10 (on pg. 39), we can determine the conductivities of the five Al_2O_3 doped IrMn thin film samples and the results obtained from the $Q - \sigma$ curve are plotted in Figure 11(b). The calculated conductivities also show an overall decreasing trend with an increase in atom content of Aluminium. As the atom content of Aluminium increased from 0.88% to 13.79%, the conductivity of the respective thin film samples were shown to decrease from $8.76 \times 10^6 \text{ S/m}$ to $2.22 \times 10^6 \text{ S/m}$. This means that the higher the doping concentration of Al_2O_3 , the lower the conductivity of the thin film sample.

As a basis for comparison, the conductivity of the Al_2O_3 doped IrMn thin film samples were also tested with the Keithley 6430Sub-FA Remote Source Meter. The conductivity of the samples were therefore tested with traditional voltammetry and the respective conductivities are also plotted against the atom content of Aluminium as shown in Figure 11(c). The overall trend observed in the measured conductivity was also decreasing with an increase in doping concentration.

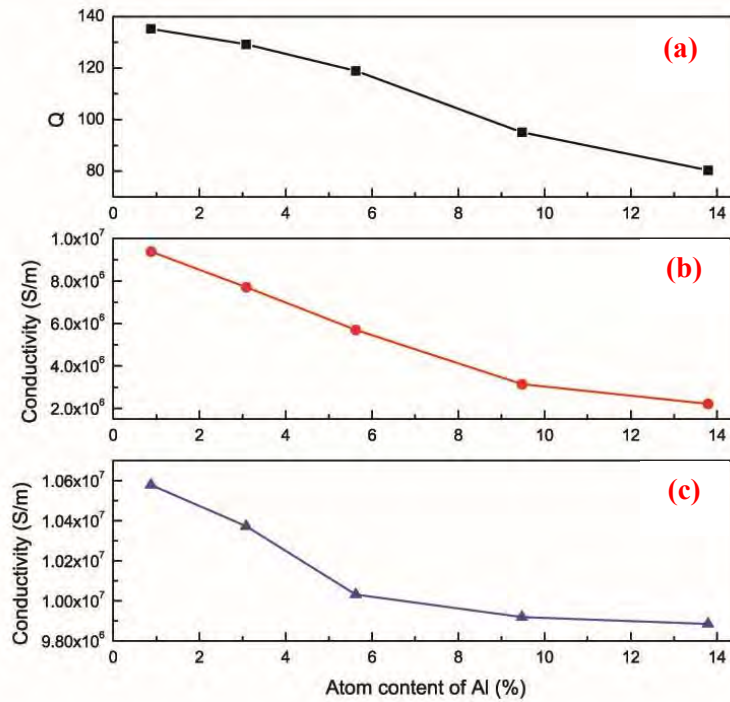


Figure 11(a): Plot of experimentally obtained quality factor against the atom content of Aluminium.

Figure 11(b): Plot of conductivity of Al₂O₃ doped IrMn thin film samples against the atom content of Aluminium. These conductivity values were quantified from the corresponding quality factors in Figure 11(a) using the simulated curve in Figure 10 (on pg. 39)

Figure 11(c): Plot of conductivity of Al₂O₃ doped IrMn thin film samples against the atom content of Aluminium. These conductivity values were tested with Keithley 6430 Sub-FA Remote Source Meter.

From this analysis, we can see that the overall trend given by the NSMM measurement of the conductivity of the Al₂O₃ doped IrMn thin film samples is consistent with the measurements made by traditional voltammetry. However, in scrutinising Figure 11(b) and 11(c), it must be noted that for a change in the DC values by a few percent, the NSMM values changed by a factor of 5. This discrepancy can be mainly attributed to the fact that the NSMM makes localised conductivity measurements at microwave frequencies on the samples being probed, while voltammetry gives average DC conductivity. In essence, the DC conductivity probes the long range motion of electrons while the AC conductivity (as measured with NSMM) probes for much shorter length scales. This indicates that NSMM is not yet ready to be a standard tool for the precise measurements of thin film conductivities and possibly other material properties as well.

Nevertheless, considering the consistency in the overall trend, NSMM has proven to be useful in offering qualitative information about the unknown conductivity of the Al₂O₃ doped IrMn thin film samples tested in a non-destructive manner and may still be considered as a method of obtaining localised measurements of the conductivities of thin film samples.

In the next section, the strength of NSMM measurements will be detailed in its potential as a means by which to give us a map of the conductivity distribution of the thin film samples under test, which is difficult to achieve using other methods.

15.3 Map of Conductivity of an Al_2O_3 doped IrMn Thin Film Sample

Using NSMM measurement, area scanning can be carried out for us to obtain a map of the conductivity distribution of a thin film sample.

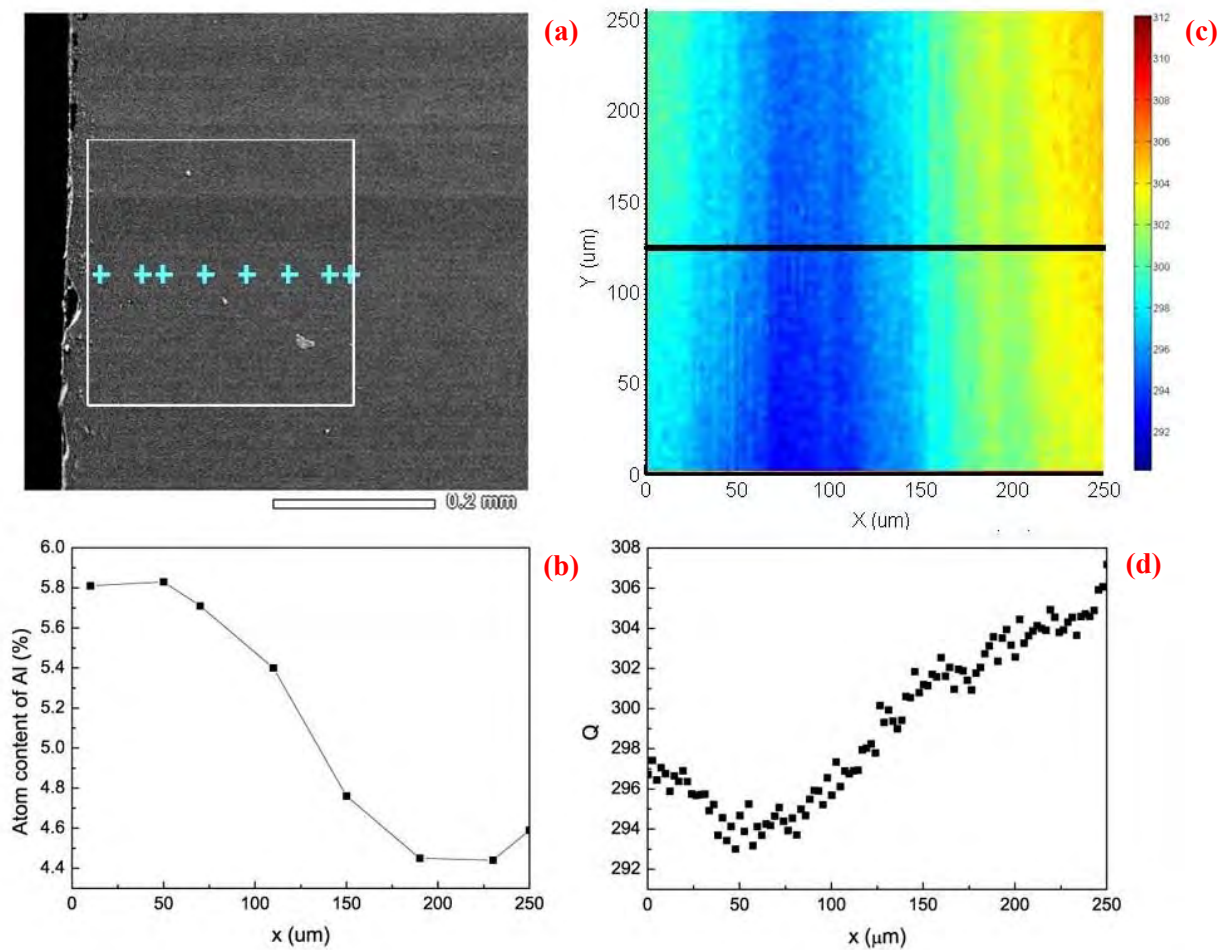


Figure 12(a): SEM image of Al_2O_3 doped IrMn thin film sample taken at the edge. The blue cross marks indicated the points at which the sample was measured by EDS while the white square outline indicate the mapped area using NSMM.

Figure 12(b): The atom content of Aluminium plotted against the arbitrary x direction.

Figure 12(c): The map of the NSMM scanned quality factor distribution over an area of $250\mu\text{m}$ by $250\mu\text{m}$ as indicated by the white square outlined in Figure 12(a). The colour bar indicates the magnitude of the quality factor.

Figure 12(d): A plot of the quality factors measured along the line in Figure 12(c). The lower the quality factor the higher the doping concentration of Al_2O_3 as is consistent with Figure 12(b).

In Figure 12(a), we have the Scanning Electron Microscope (SEM) image taken at the edge of the Al_2O_3 doped IrMn thin film sample. The blue cross marks indicate the eight points on the film at which the sample was measured by EDS while the white square outlined indicates the area scanned by the NSMM experimental setup. From this image, not much is told to us about the properties of the thin film.

In Figure 12(b), the atom content of Aluminium as measured by the EDS at the points indicated on Figure 12(a) is plotted against the arbitrary x direction. Along the line of points spanning a length of only $250\mu\text{m}$, we can see that the atom content of Aluminium already changes significantly and is not uniform at all. Since the conductivity of the thin film sample is inversely related to the Aluminium content (as found in the previous section), the conductivity measured using the NSMM technique would also vary from point to point. This explains why the localised NSMM measurements of conductivity vary so significantly from the voltammetry measurements which are taken as an average value over the entire thin film sample.

In Figure 12(c) we see the NSMM scanned quality factor distribution over an area of $250\mu\text{m}$ by $250\mu\text{m}$ as indicated by the white square outlined in Figure 12(a). Also, as indicated by the colour bar, the colour on the map indicates the magnitude of the quality factor Q at every point in the mapped region. The higher up the colour bar, the higher the quality factor Q measured. The individual quality factors measured along the line drawn across Figure 12(c) are plotted in Figure 12(d).

In accordance with the trend in Figure 11(a) (on pg. 42), the higher the doping concentration of Al_2O_3 , the lower the measured quality factor and the lower the local conductivity of the thin film sample. This is clearly illustrated in Figures 12(b) and 12(d) where a higher atom content of Aluminium measured by EDS corresponds to a lower quality factor Q measured by NSMM. In this way, we can conclude that the map of the quality factor distribution is consistent with the actual composition of the thin film sample and is a reliable means of mapping the conductivity of the thin film sample.

Hence, we see that NSMM has the ability to give us localised measurements of the quality factor Q and resonant frequency f_r which can then be related to the electrical properties of the samples being measured. In addition, a map of the distribution of the electrical property, e.g. conductivity can be obtained, making NSMM imaging one of a kind.

Chapter V

Further study with Simulations

We found out from the works by Huang [19] and Anlage et Al. [10] that the geometry of the tip and tip size play an important role in determining the radiation distribution of the microwaves as well as the corresponding impedance contribution from the tip-sample interaction respectively. Using the same simulations described in Chapter IV Section 15.1, the effect of various tip properties and tip-sample configurations on the sensitivity and spatial resolution of the probe are studied.

The use of computerised simulations has proven very useful in this aspect as it is not feasible to fabricate tips of various geometries and sizes to investigate the corresponding effects experimentally. With COMSOL Multiphysics, many different tip sample geometries could be drawn and solved using the finite element method in order for us to simulate the resonant frequency shifts and quality factor changes. Our investigation will cover the probing of metallic films with metallic tips and the probing of dielectric films with CNT bundled tips.

In this chapter, we will look at how the parameters were calibrated and some of the tip-sample configurations modelled before using the simulated data to analyse the sensitivity and spatial resolution of the different configurations.

16 Simulation Methodology

16.1 Calibration of Parameters

The simulated frequency shift can be expressed as follows:

$$\frac{\Delta f_r}{f_r} = \frac{E_{pert}}{\alpha} \quad (38)$$

$$\frac{f_{r(sample)} - f_{r(air)}}{f_{r(sample)}} = \frac{E_{sample} - E_{air}}{\alpha} \quad (39a)$$

For calibration purposes, looking at the RHS of the equation, the resonant frequency values are taken as experimentally determined values and as illustrated in Equation (38a), we see that the resonant frequency shift is found by taking the difference between the resonant frequency measured over the sample and the resonant frequency measured in air. On the LHS of the equation, E_{pert} represents the difference between simulated electrical energy density data taken over a sample and the simulated electrical energy density data taken in air. These values of electrical energy density can be quantified by the integration over all domains of the tip-sample geometry.

The magnitude of the constant α represents the energy coupled by the resonator cavity over its surroundings. The calibration of this constant was carried out by using experimental data corresponding to a 10 μ m radius Copper tip or a 10 μ m CNT bundled tip and the set of simulated data corresponding to the experimental configurations respectively.

$$\text{For metallic tips, } \alpha = -2.573 \times 10^{-17} J$$

$$\text{For CNT bundled tips, } \alpha = -1.352 \times 10^{-13} J$$

(The negative sign is included in the calibration constant purely for consistency since Δf is a negative value.)

The simulated quality factor Q can be expressed in a form already familiar to us as it was used in the analysis in Chapter III Section 15.1. For the quality factor measured over a sample, we have Equations (36) and (37):

$$Q_{air} = 2\pi f_{r(air)} \frac{E_{total}}{P_{cavloss} + P_{tip-air loss}} \quad (40)$$

$$\begin{aligned}
& Q_{sample} \\
& = 2\pi f_{r(sample)} \frac{E_{total}}{P_{cavloss} + P_{tip-sample loss} + P_{resis. heat over sample}} \quad (41)
\end{aligned}$$

For calibration purposes, Q_{sample} and $2\pi f_{r(sample)}$ can be taken as experimentally determined values. On the LHS of the equation, $P_{tip-sample loss}$ can be quantified by the integration along the tip boundary while $P_{resis. heat over sample}$ can be quantified by the integration over all domains of the tip-sample geometry.

In the same way, the constants E_{total} and $P_{cavloss}$ which are independent of sample properties can then be calibrated as well. The calibration of these constants were also carried out by using the experimental data corresponding to a 10 μ m radius Copper tip or a 10 μ m CNT bundled tip and the corresponding sets of simulated data.

$$\text{For metallic tips, } E_{total} = 3.541 \times 10^{-16} J \text{ and } P_{cavloss} = 2.168 \times 10^{-8} W$$

$$\text{For CNT bundled tips, } E_{total} = 2.677 \times 10^{-15} J \text{ and } P_{cavloss} = 2.494 \times 10^{-7} W$$

With the aforementioned parameters calibrated, we can then carry out simulations for all sorts of tip-sample configurations and obtain the corresponding simulated resonant frequency shifts and quality factors related to these configurations.

16.2 Tip-sample Configurations and Parameters

For each tip-sample configuration, a model can be drawn on COMSOL Multiphysics which is then meshed into a finite number of elements and solved. For visualisation purposes, some examples of the models used are detailed below. It must be noted that all models are drawn on the RF module in the 2D axial symmetric mode.

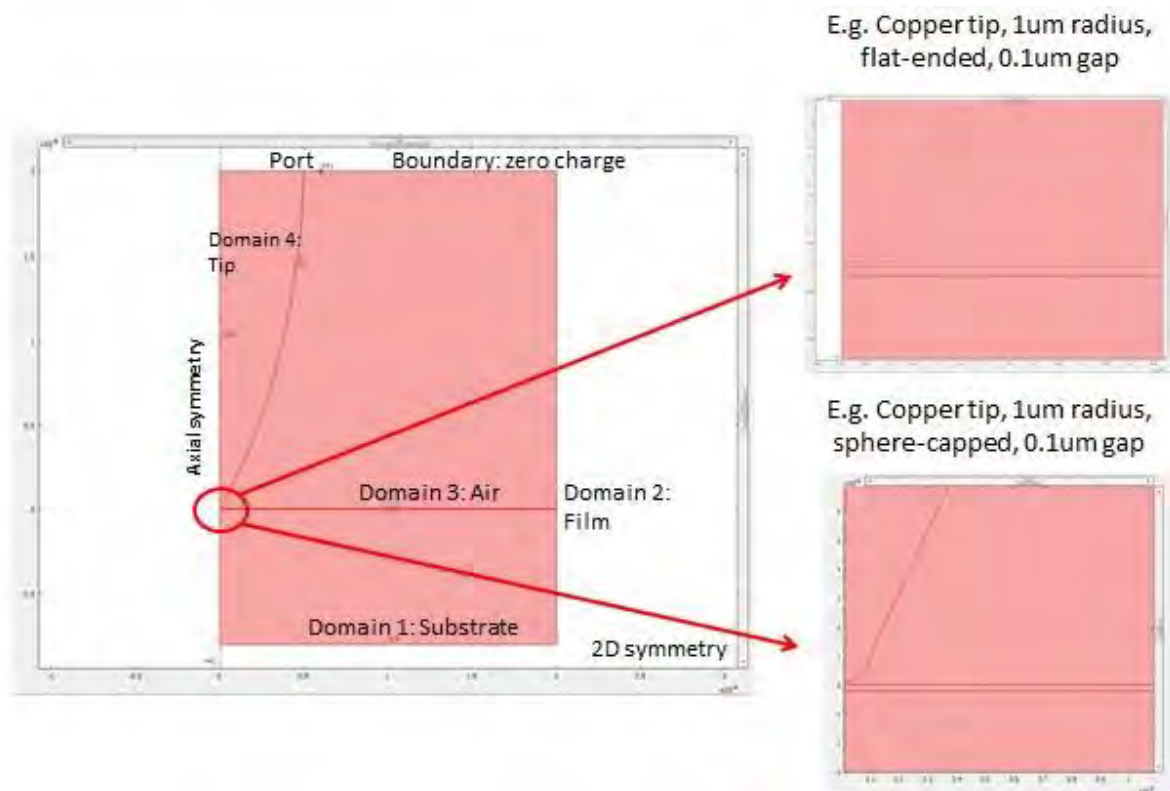


Figure 13: The tip sample configuration for 1 μm Copper tip held 0.1 μm above a metallic thin film sample and substrate. In the insets, the difference between the flat-ended tip and the sphere-capped tip are illustrated as an example of how the tip-sample configuration can be modified.

In Figure 13, we see the general configuration used for the probing of metallic samples with metallic tips. The tip shown above is a copper tip of 1 μm radius at the apex, held 0.1 μm above the sample. By making isolated changes to the configuration showed above, we can investigate the effects of different parameters. Shown in the insets are examples of different shaped tips, i.e. the flat-ended tip and the sphere-capped tip respectively. By changing only one parameter at a time, the effects of the following parameters will be explored:

- Tip radius
- Tip-sample distance
- Tip shape
- Tip material

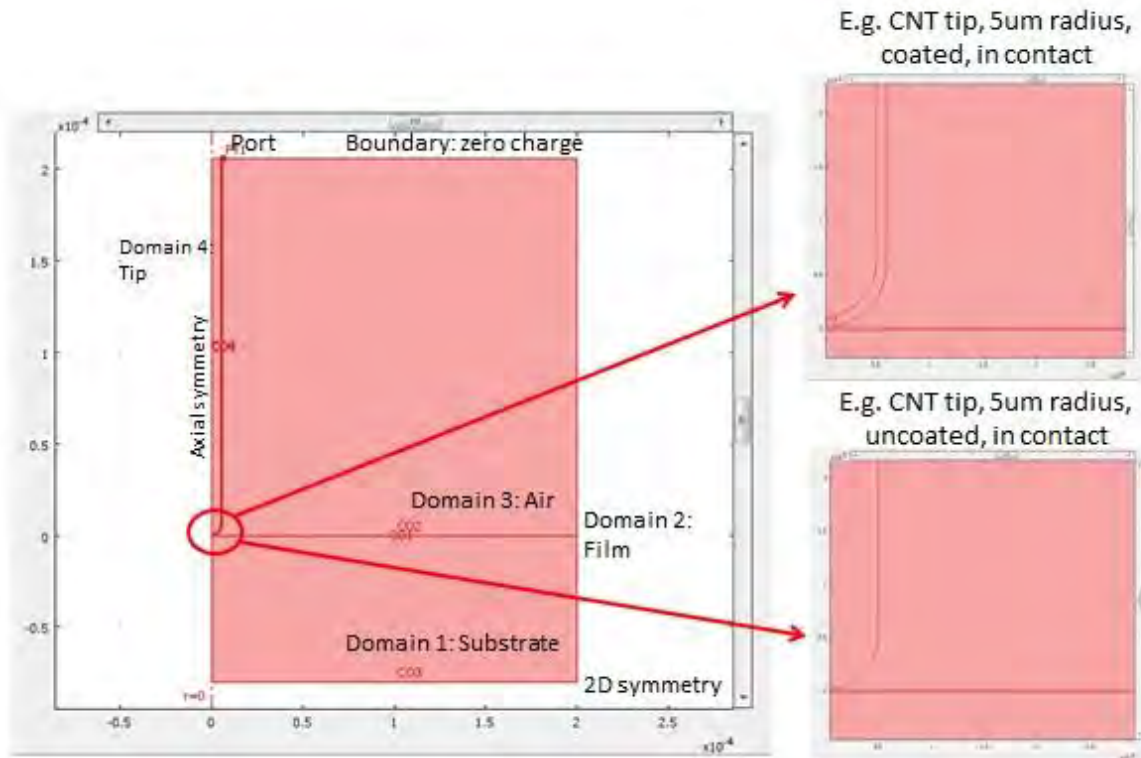


Figure 14: The tip sample configuration for 5 μm CNT tip in contact mode with a dielectric thin film sample and substrate. In the insets, the difference between the a coated tip and an uncoated tip are illustrated as an example of how the tip-sample configuration can be modified.

In Figure 14, we see the general configuration used for the probing of dielectric samples with CNT bundled tips. The tip shown above have a radius of 5 μm and are in contact mode with the sample. By making isolated changes to the configuration shown above, we can investigate the effects of different parameters. Shown in the insets are examples of a coated tip and an uncoated tip in contact with the thin films being probed. By changing only one parameter at a time, the effects of the following parameters will be explored:

- Tip radius
- Coating on the tip

Experimentally, the CNT bundled tip is normally used in sweeping mode on the sample due to the flexibility of the bundle in sweeping over the samples. However, due to the inability to model the CNT tip in sweeping mode in a 2D axial symmetric model, the simulations carried out in this study are limited to tip-sample distances at or larger than contact mode so that the tip can be considered as a cylindrical symmetrical bundle as shown in Figure 14.

16.3 Determining Sensitivity and Spatial Resolution

In order to determine the sensitivity of the probe tip, the plot of the resonant frequency or quality factor against other parameters such as conductivity of metallic films, relative permittivity of dielectric films or tip-sample distance can be used and analysed. By finding the extent of the Δf_r or ΔQ with respect to the corresponding parameter (i.e. σ , ϵ or tip-sample distance), the sensitivity of each model can be found.

An example is illustrated in Figure 15 below. In the plot on the left, we see the variation of the quality factor Q over the large range of conductivities. The plot on the right corresponds to the rate of change of the quality factor Q over the same range of conductivities and we can see that the sensitivity for the model with a $0.1\mu\text{m}$ gap is better than that of the model with a $1\mu\text{m}$ gap since the ΔQ is over a larger range.

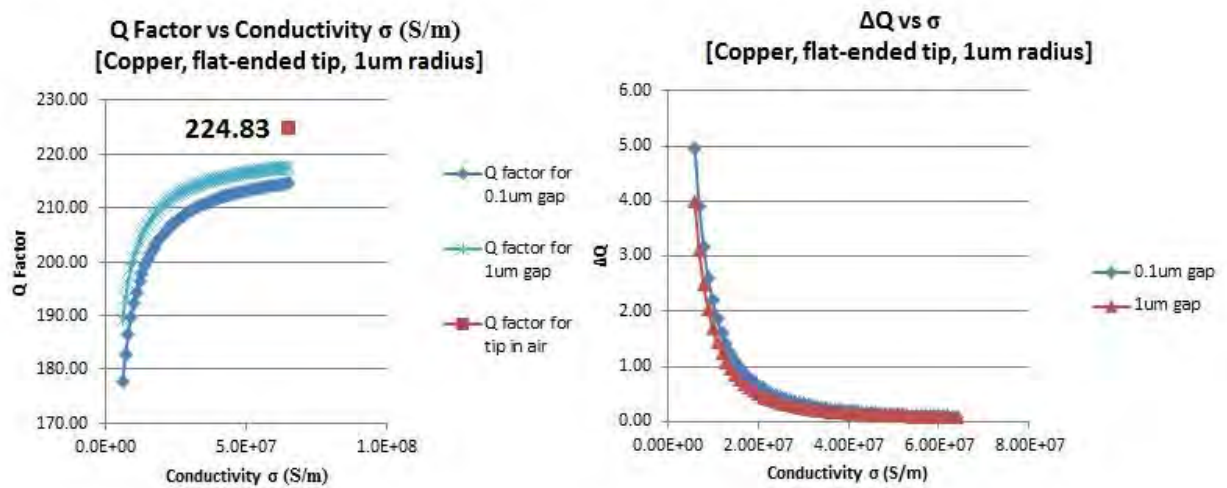


Figure 15: The plot of quality factor Q versus conductivity as well as the corresponding plot of ΔQ versus conductivity used in the analysis of the sensitivity of the model. Here the models under comparison are for a metallic, flat-ended, $1\mu\text{m}$ radius Copper tip at tip-sample distances of $0.1\mu\text{m}$ and $1\mu\text{m}$ respectively.

In our analysis, the determination of the sensitivity of each tip-sample configuration was carried out based on the comparison between different configurations. Thus, the plots used for comparison and the corresponding conclusions are included in Table 1 in the following section.

As for the spatial resolution achieved by each tip, we look at the cross-section line plots of the electrical energy density along the boundary of the thin film sample and air domain. From these plots, the Full Width at Half Maximum (FWHM) approach is then used to determine the spatial resolution of each model.

Since the simulation model is symmetric about the vertical axis, the data points corresponding to the electric energy density can be reflected in the y-axis. In this case, the negative distance values purely indicate a reflection of the tip-sample geometry in the vertical axis.

In the example in Figure 16 below, the geometry of the tip-sample configuration is as such: CNT bundled tip with $5\mu\text{m}$ radius and $0.5\mu\text{m}$ layer coating held in contact with the sample. Taking the Full Width at Half Maximum, the spatial resolution is then determined to be $3.38\mu\text{m}$ for this model.

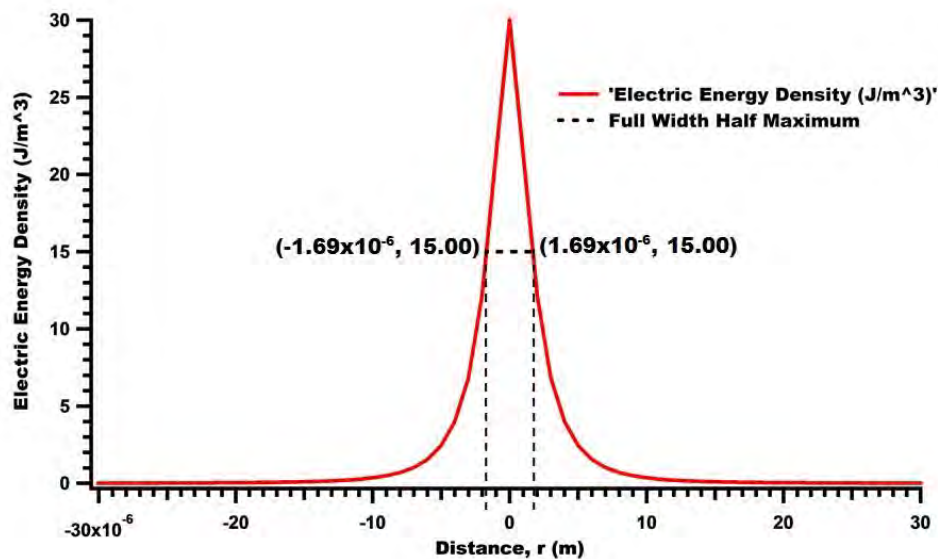


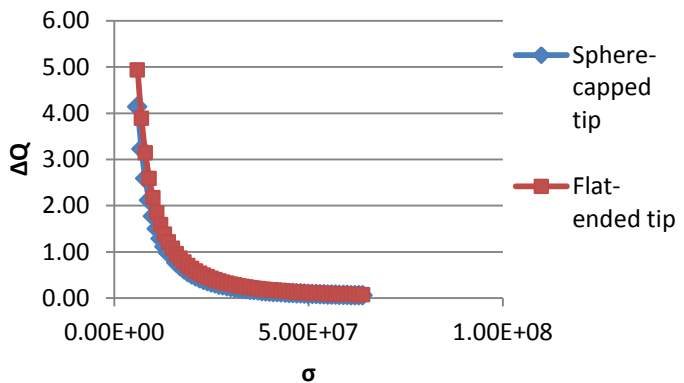
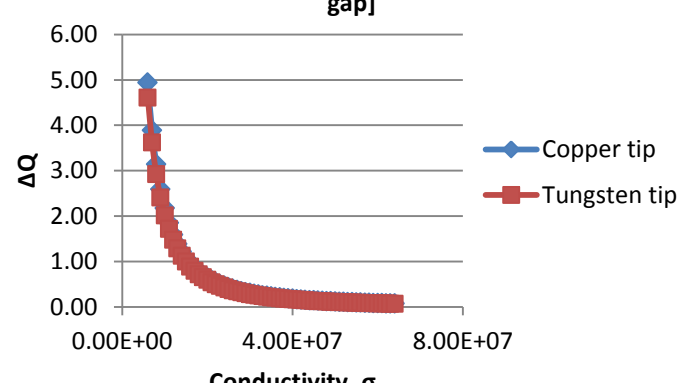
Figure 16: Plot of the electrical energy density against distance, r along the boundary of the thin film sample and air domains. Included in the plot is the Full Width Half Maximum (FWHM) analysis. For this plot, the geometry of the tip-sample configuration is as such: CNT bundled tip with $5\mu\text{m}$ radius and $0.5\mu\text{m}$ layer coating held in contact with the sample. The spatial resolution is found to be $3.38\mu\text{m}$.

In our analysis, the spatial resolution values are easily quantified and the procedure is repetitive for all configurations studied. Hence, in Table 1 in the following section, only the numerical values of the spatial resolution will be listed while the individual plots can be found in the Appendix. The smaller the numerical value, the higher the spatial resolution achieved.

17 Simulation Results

17.1 Table of Results for Various Tips on Various Thin Film Samples

Metallic tips on metallic thin film samples - Effect of tip radius		
Tip radius	Sensitivity	Spatial Resolution
1 μm	<p style="text-align: center;">ΔQ vs $\Delta\sigma$ [Parameters: Copper tip, flat-ended, 0.1 μm gap]</p> <p style="text-align: center;">The smaller the radius of the tip, the greater the sensitivity of the tip.</p>	2.58 $\mu\text{m}^{(1)}$
5 μm		15.94 $\mu\text{m}^{(2)}$
10 μm		30.40 $\mu\text{m}^{(3)}$
Metallic tips on metallic thin film samples - Effect of tip-sample distance		
Tip-sample distance	Sensitivity	Spatial Resolution
100nm	<p style="text-align: center;">ΔQ vs $\Delta\sigma$ [Parameters: Copper tip, flat-ended, 1 μm radius]</p> <p style="text-align: center;">The smaller the tip-sample distance, the greater the sensitivity of the tip.</p>	2.58 $\mu\text{m}^{(1)}$
1 μm		2.86 $\mu\text{m}^{(4)}$

Metallic tips on metallic thin film samples - Effect of tip shape		
Tip shape	Sensitivity	Spatial Resolution
Sphere-capped	<p style="text-align: center;">ΔQ vs σ [Parameters: Copper tip, 1μm radius, 0.1μm gap]</p>  <p>The flat-ended tip showed a slightly greater sensitivity compared to the sphere-capped tip.</p>	1.04 $\mu\text{m}^{(5)}$
Flat-ended		2.58 $\mu\text{m}^{(1)}$
Metallic tips on metallic thin film samples - Effect of tip material		
Tip material	Sensitivity	Spatial Resolution
Copper	<p style="text-align: center;">ΔQ vs $\Delta\sigma$ [Parameters: Flat-ended tip, 1μm radius, 0.1μm gap]</p>  <p>The sensitivity of the Copper tip was slightly better than that of the Tungsten tip.</p>	2.58 $\mu\text{m}^{(1)}$
Tungsten		2.58 $\mu\text{m}^{(6)}$

CNT bundled tips on dielectric thin film samples- Effect of tip radius		
Tip radius	Sensitivity	Spatial Resolution
1µm	<p style="text-align: center;">Δf vs Δtip-sample distance [Parameters: CNT bundled tip, 1µm coating layer, in contact mode]</p> <p style="text-align: center;">The 1µm radius tip shows a greater sensitivity than the 5µm radius tip.</p>	1.36µm ⁽⁷⁾
5µm		4.60µm ⁽⁸⁾
CNT bundled tips on dielectric thin film samples - Effect of coating of tip		
Coated or uncoated	Sensitivity	Spatial Resolution
Coated	<p style="text-align: center;">Δf vs Δtip-sample distance [Parameters: CNT bundled tip, 5µm radius, 0.5µm coating/ air layer, in contact mode]</p> <p style="text-align: center;">The tip with a 0.5µm coating showed greater sensitivity than the uncoated tip at the same effective distance.</p>	3.38µm ⁽⁹⁾
Uncoated		6.36µm ⁽¹⁰⁾

Table 1: Table of results detailing the sensitivity and spatial resolution achieved by each tip-sample configuration for metallic films being probed by metallic tips and dielectric films being probed by CNT bundledtips.

17.2 Discussion on the Sensitivity and Spatial Resolution

As can be seen from the results in Table 1 above, the general guidelines to consider when deciding on tip parameters would be the tip shape, size (in terms of radius), the tip-sample distance and the material of the tip (i.e. Metallic or CNT tips with or without coating) as these affect the sensitivity and spatial resolution achieved. From the findings, it can be concluded that the tip should be fabricated with an apex as small as physically possible and maintained at the smallest tip-sample distance in order to achieve high sensitivity and high spatial resolution at the same time. On the other hand, the material chosen for the metallic tip (i.e. Copper or Tungsten) is not as important. In some cases, Tungsten tips are preferred as they are harder and more robust than Copper tips.

In his works, Huang [8], [9] found that the tip is inevitably flattened when it comes into contact with the sample being probed. This was evidenced from the SEM images of the tips used, taken before and after measurement. Not only that, he found that a flatter tip yielded a better sensitivity while a sharper spherical tip gave a higher spatial resolution. Our results were consistent with his study and so we also found that the flatter the tip, the better the sensitivity but the spherical-capped tip gave a higher spatial resolution. In this respect, the tip geometry has to be optimised in order to balance the trade-off between high sensitivity and high spatial resolution.

Also, considering the use of CNT bundles attached onto a metallic tip in contact or soft contact mode only, we see a similarity in that the smaller the size of the tip, the better the sensitivity and the higher the spatial resolution. However, it must be noted that the CNT tip gives a much higher spatial resolution than the metallic tips for apexes of the same size. In addition, using the same model and by changing the layer of non-conductive dielectric coating into a layer of air and maintain the same tip-sample distance, we see that the effect of the dielectric coating is desirable as it improves both the sensitivity and the spatial resolution achieved.

From the study with simulations, it is evident that in the near-field regime, the spatial resolution is no longer determined by the wavelength of the radiation used, instead, it is given by the tip size, shape, material and tip-sample distance. The geometry of the tip is therefore an important factor to consider for microscopy techniques such as NSMM.

Chapter VI

Conclusion and Future Work

In this report, the fundamentals behind near-field scanning techniques were studied in detail and used as a basis for the development of a home-designed near-field scanning microwave microscopy system, consisting of a sharpened metal tip, mounted on the centre conductor of a high quality (Q) $\lambda/4$ coaxial resonator with microwave energy supplied to the probe setup via a VNA. By taking advantage of the near-field regime, the Abbe diffraction limit for electromagnetic radiation is overcome and high resolution measurements can be made. The measurement data was acquired in the form of shifts in the resonant frequency f_r and changes in the quality factor Q when samples were placed under test.

By building up a simulation model on COMSOL Multiphysics, a computational platform, we were able to extract material properties of interest, namely the conductivity of the samples under test, from the measured data. This was done by first validating the simulation model with measurements of standard metallic thin film samples and then obtaining a relationship curve between the change in quality factor Q and conductivity. Using the simulated curve, measurement data taken over the samples of unknown conductivity could then be related to the corresponding conductivity values thus localised measurements and a mapping of the conductivity distribution of thin film samples of unknown conductivity distribution could be achieved.

Hence in this project, NSMM was employed as a tool for non-destructive characterisation of localised material electrical properties, such that the distribution of electrical properties on thin film samples can be found. In addition, the conductivity distribution in terms of quality factor Q was mapped, making this method one of a kind in imaging the material properties of the samples under test.

Using simulations to further study the effects of various parameters on the spatial resolution and sensitivity achieved, we see that the optimisation of the geometry of the tip and sample are integral to attaining results with high sensitivity and high spatial resolution. In general, the smaller the tip and the tip-sample distance, the better the sensitivity and spatial resolution. In this way, the simulations were meaningful in helping us to better understand the workings of the NSMM system.

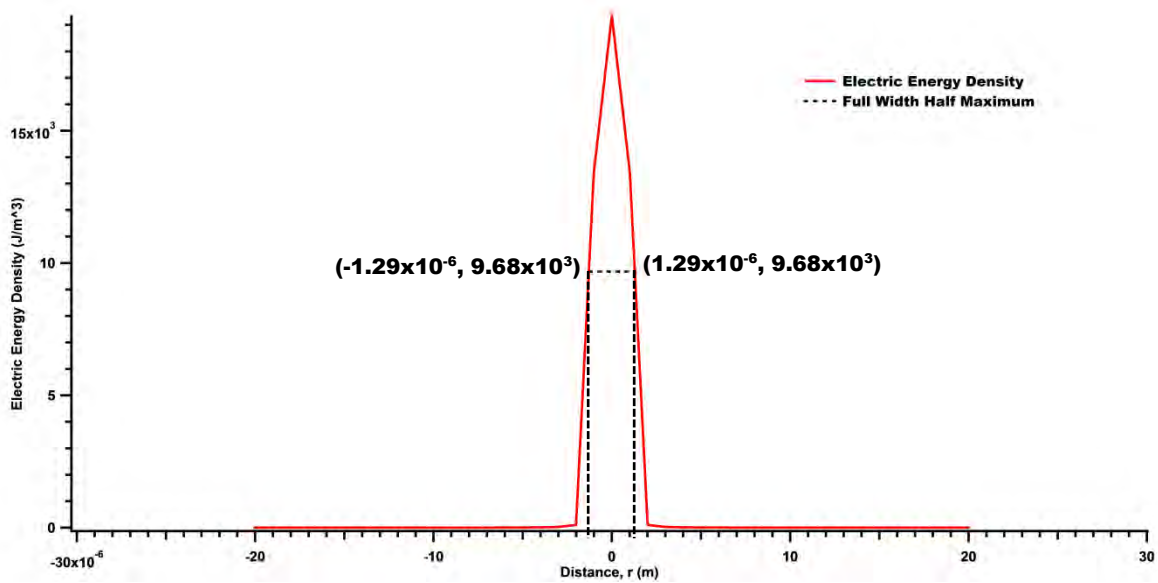
NSMM is fundamentally a tool for physicists to learn more about the properties of materials, and so the motivations behind its development stem from the need to be able to characterise, quantitatively determine and map the electrical properties of said materials. This makes NSMM applicable on the production line in determining uniformity and homogeneity of fabricated thin films used in semiconductors and other devices. As the method is continually being developed, a promising future direction the team at CSMM is embarking on would be to employ the penetration abilities of microwaves in applying NSMM in the biomedical field so as to be able to characterise cells and other biological materials, providing a potential alternative to the more mature but also more harmful method of using X-rays.

Appendix

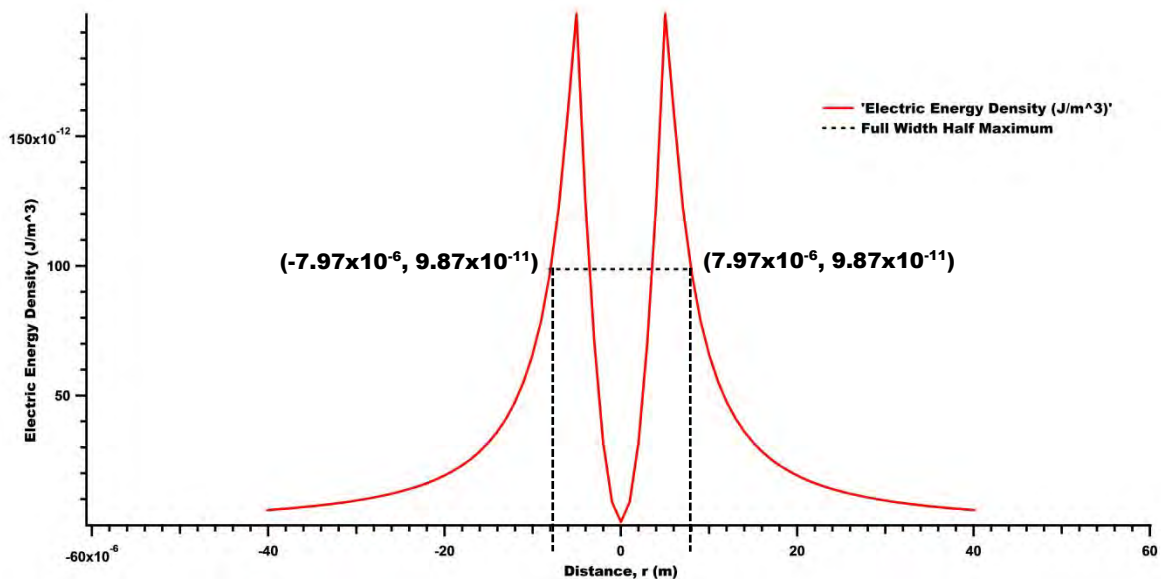
Determination of Spatial Resolution

The cross-section line plots of the electrical energy density along the boundary of the thin film sample and air domains were extracted from the simulation. From these plots, the Full Width at Half Maximum (FWHM) approach is used to determine the spatial resolution of each model.

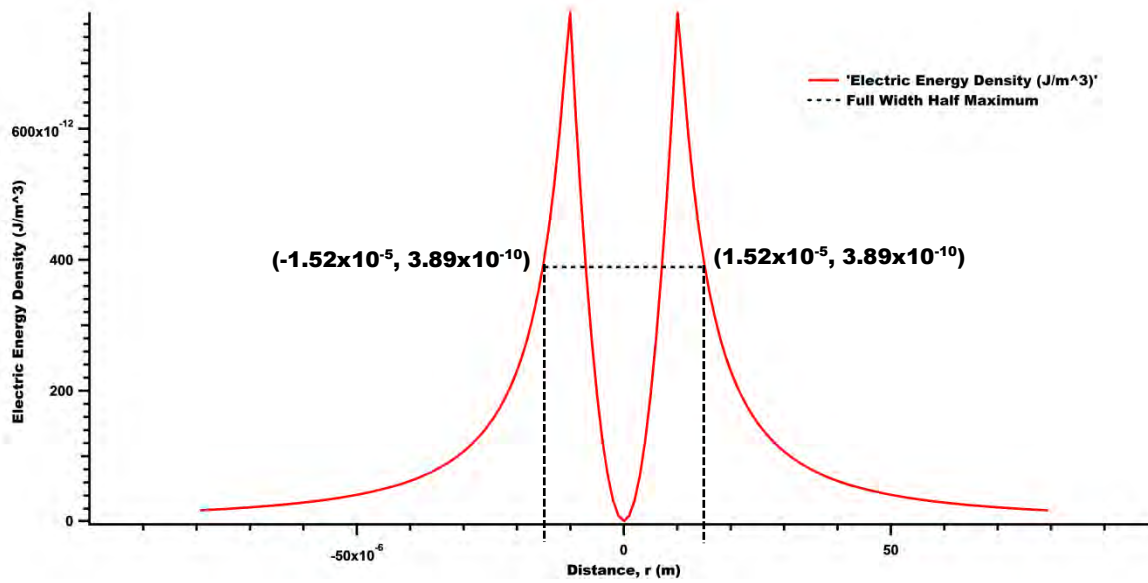
- (1) Parameters: Copper tip, flat-ended, 1 μm radius at 100nm tip-sample distance
Spatial Resolution: 2.58 μm



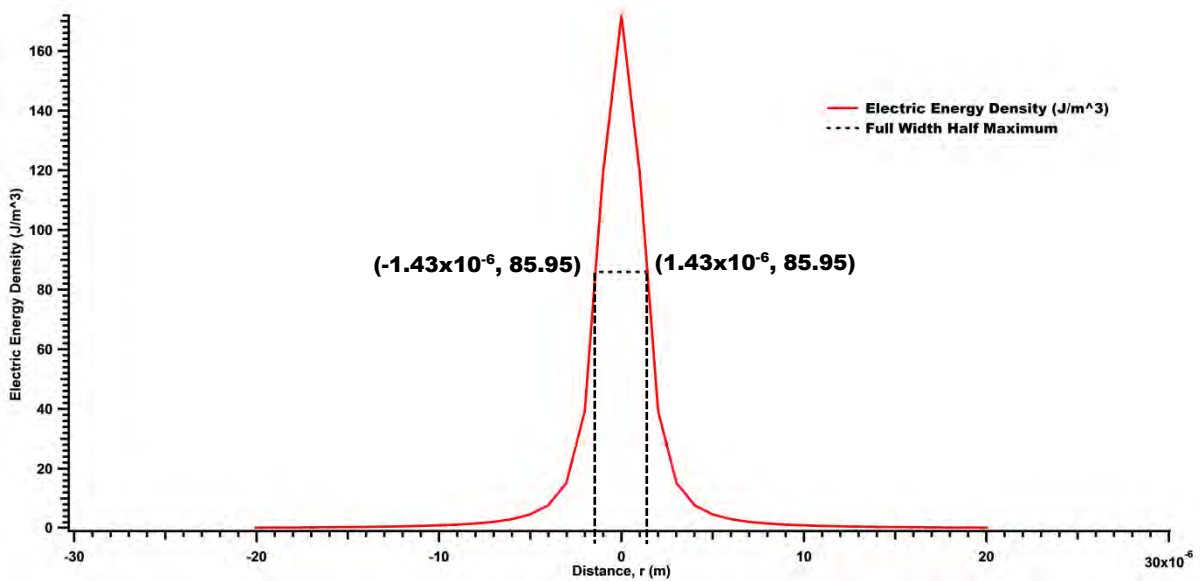
- (2) Parameters: Copper tip, flat-ended, 5 μm radius at 100nm tip-sample distance
Spatial Resolution: 15.94 μm



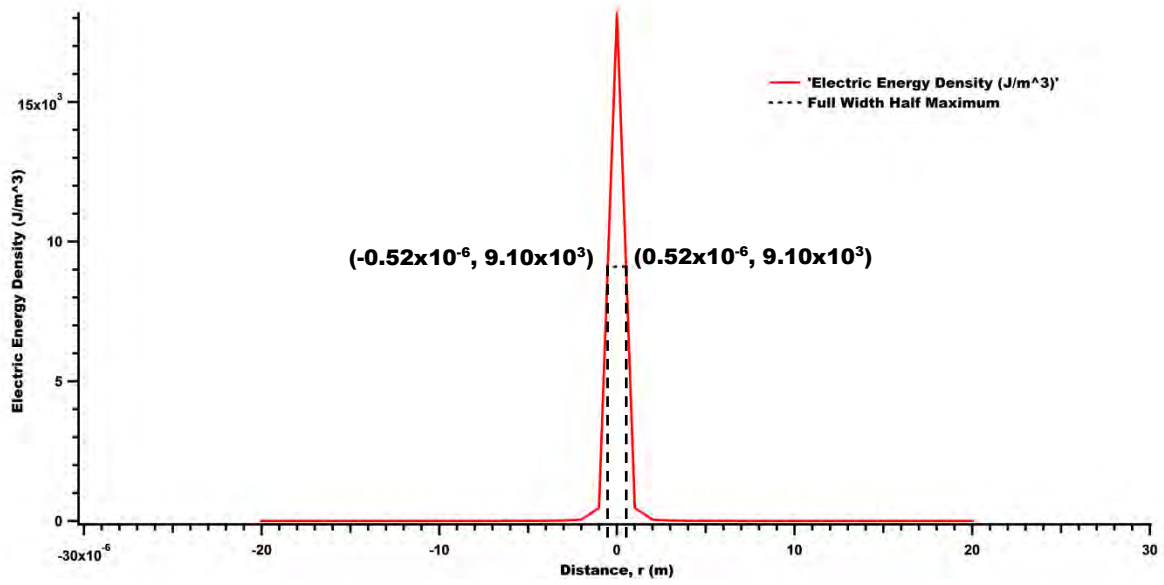
- (3) Parameters: Copper tip, flat-ended, 10 μm radius at 100nm tip-sample distance
 Spatial Resolution: 30.40 μm



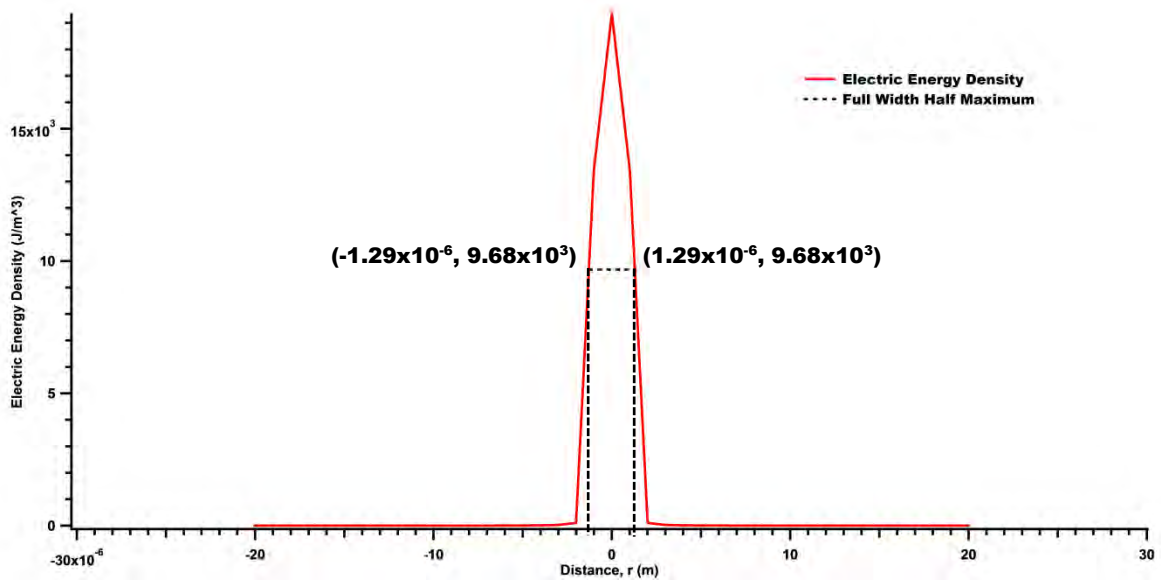
- (4) Parameters: Copper tip, flat-ended, 1 μm radius at 1 μm tip-sample distance
 Spatial Resolution: 2.86 μm



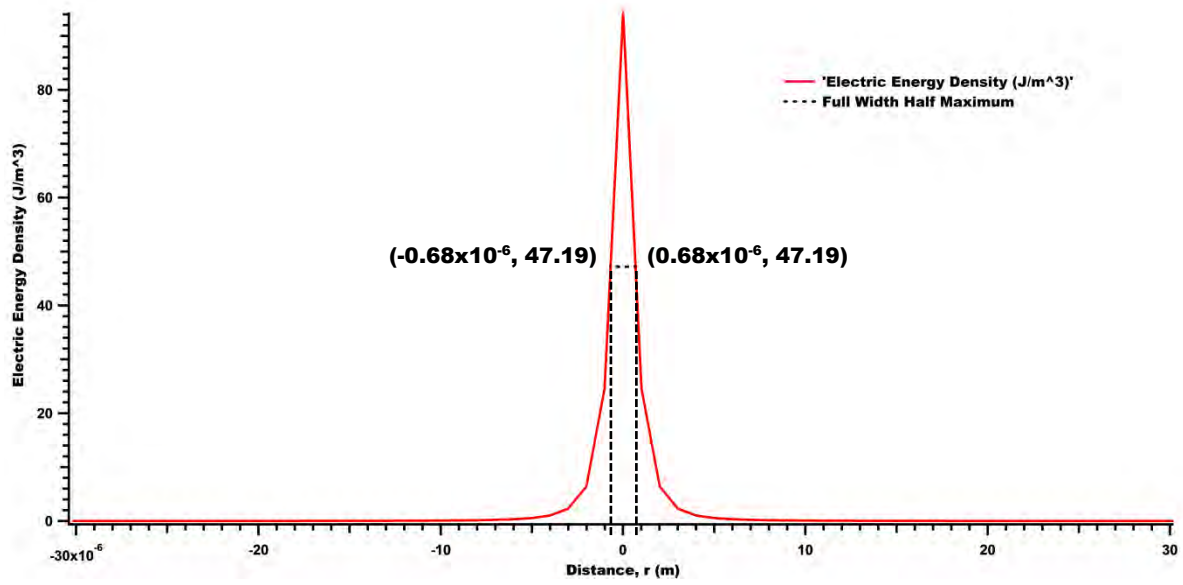
(5) Parameters: Copper tip, sphere-capped, 1 μm radius at 100nm tip-sample distance
Spatial Resolution: 1.04 μm



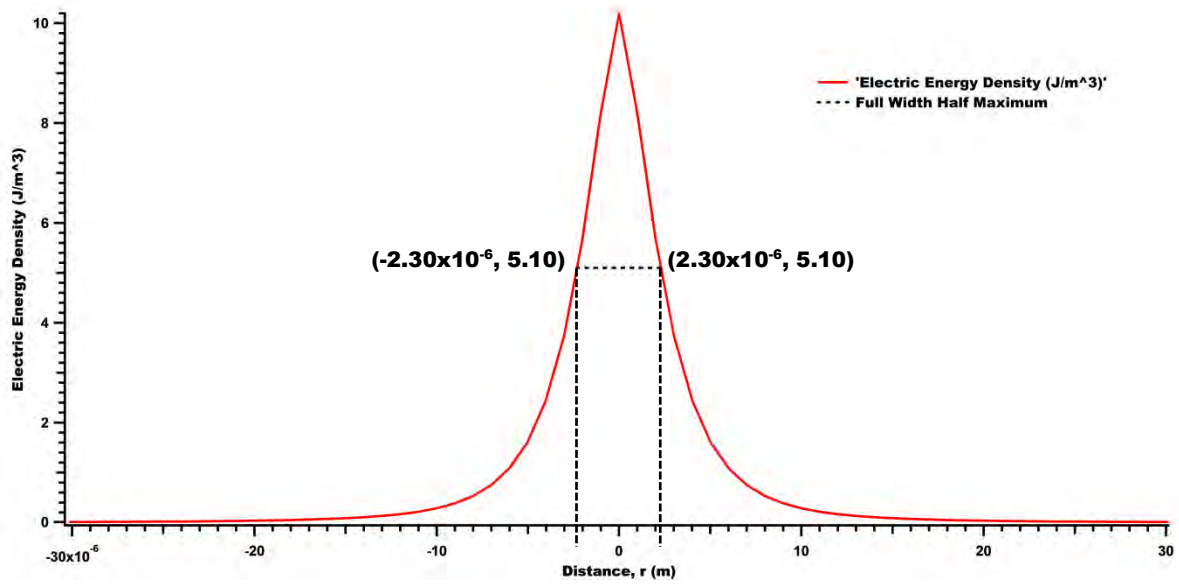
(6) Parameters: Tungsten tip, flat-ended, 1 μm radius at 100nm tip-sample distance
Spatial Resolution: 2.58 μm



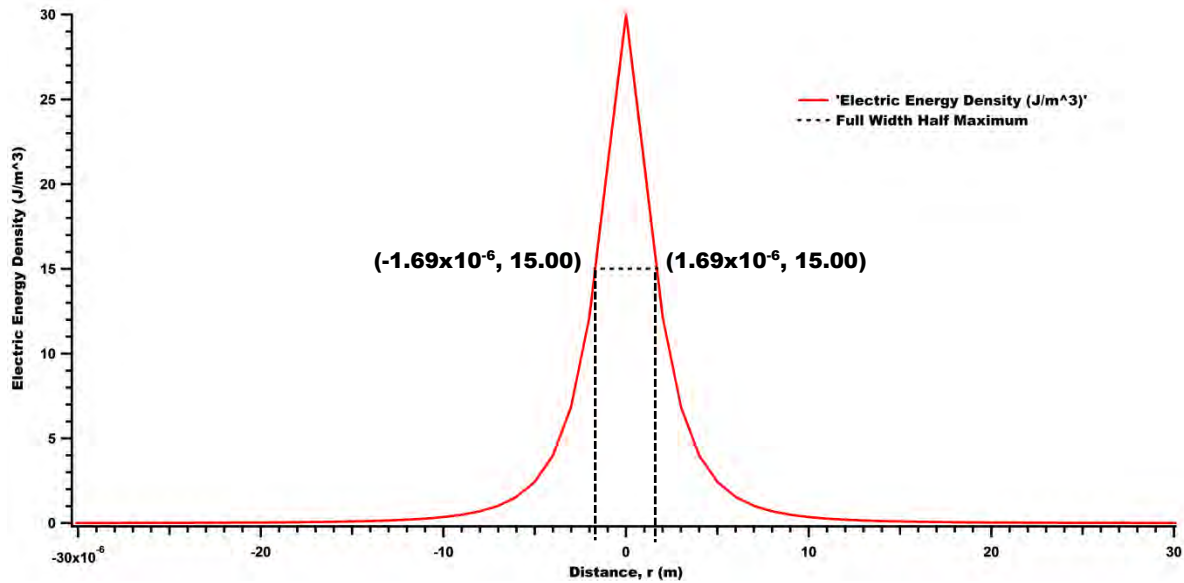
(7) Parameters: CNT bundled tip, 1 μm radius, 1 μm coating in contact mode
Spatial Resolution: 1.36 μm



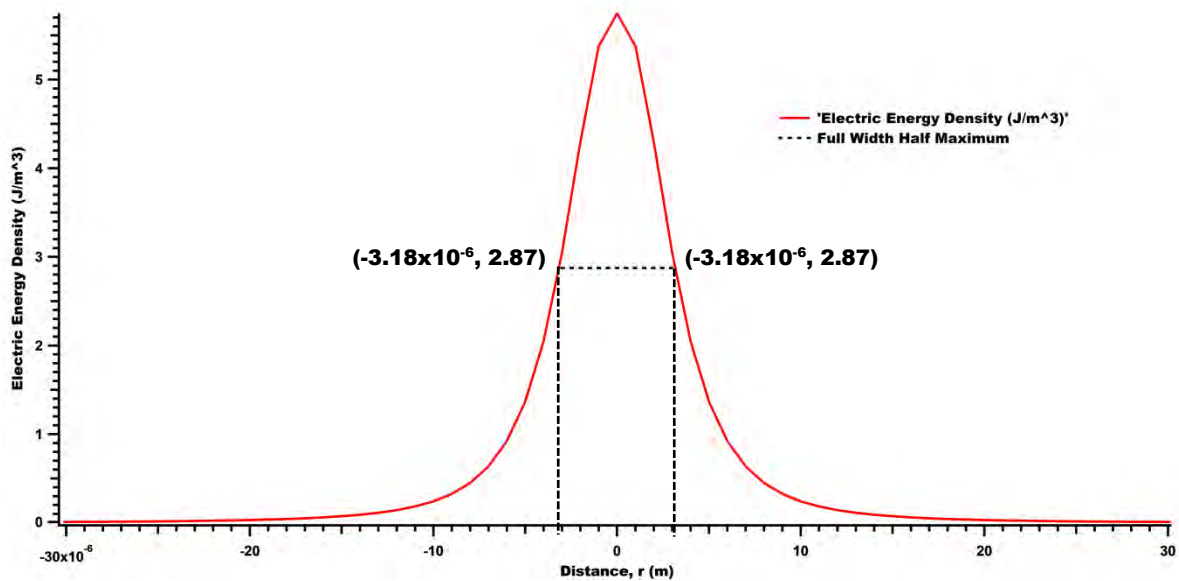
(8) Parameters: CNT bundled tip, 5 μm radius, 1 μm coating in contact mode
Spatial Resolution: 4.60 μm



(9) Parameters: CNT bundled tip, $5\mu\text{m}$ radius, $0.5\mu\text{m}$ dielectric coating layer, in contact mode
Spatial Resolution: $3.38\mu\text{m}$



(10) Parameters: CNT bundled tip, $5\mu\text{m}$ radius, $0.5\mu\text{m}$ air layer (in place of dielectric coating) in contact mode
Spatial Resolution: $6.36\mu\text{m}$



References

- [1] Synge, E. H. "A suggested method for extending microscopic resolution into the ultra microscopic region." *Philos. Mag. Jour. Sci.* 6.35 (1928): 356-362.
- [2] Bethe, H. A. "Theory of Diffraction by Small Holes." *Phys. Rev.* 66.7-8 (1944): 163.
- [3] Bouwkamp, C. J. "On Bethe's theory of diffraction by small holes." *Philips Res. Rep.* 5.5 (1950): 321-332.
- [4] Massey, G. A. "Microscopy and pattern generation with scanned evanescent waves." *Appl. Optics* 23.5 (1984): 658-660.
- [5], [16] Novotny, L. "The History of Near-field Optics." *Progress in Optics* 50 (2007): 137 - 184.
- [6] Soohoo, R. F. "A Microwave Magnetic Microscope." *Appl. Phys* 33.3 (1962): 1276-1277.
- [7], [18], [37] Wang, Zhengyu, et al. "Quantitative measurement of sheet resistance by evanescent microwave probe." *App. Phys. Lett.* 86.15 (2005): 153118.
- [8] Huang, Shuogang, H. M. Christen and M.E. Reeves. "Parameter-free extraction of Thin-Film Dielectric Constant from Scanning Near Field Microwave Microscope Measurements." *American Phys. Soc.* arXiv:0909.3579 (2009).
- [9], [11], [33], [35] Anlage, S. M., V. V. Talanov and A. R. Schwartz. "Principles of near-field microwave microscopy." *Scanning probe microscopy* (2007): 215-253.
- [10], [19] Huang, Shuogang. *Thin Film Dielectric Properties Characterization by Scanning Near-Field Microwave Microscopy*. Dissertation for degree of Doctor of Philosophy. George Washington University. Washington D. C.: ProQuest LLC, 2009.
- [12], [13] Griffiths, D.J. & Reed College. *Introduction to electrodynamics. Vol. 3*. Upper Saddle Rive, NJ: prentice Hall, 1999.
- [14] Born, M and E. Wolf. *Principles of Optics*. Pergamon Oxford, 1980.
- [15] Lipson, S. G & Lipson, H. *Optical physics*. Cambridge University Press, 1995.
- [17] Chisum, J. D., Popovic, Z. "Performance limitations and measurement analysis of a near-field microwave microscope for nondestructive and subsurface detection." *Microwave Theory and Techniques, IEE Transactions on* 60.8 (2012): 2605-2615.
- [20], [21], [36] Jackson, John David. *Classical Electrodynamics, 3rd edition*. New York: Wiley, 1999.
- [22] Wang, X. *Near-field Microwave Microscopy for Thin Film Characterisation*. Thesis for Degree of Bachelor of Science with Honours. Singapore, 2008.

- [23] Osofsky, S. S. and S. E. Swarz. "IEEE Trans." *Microwave Theory Tech* 40.1701 (1992).
- [24] Caloz, C. and T. Itoh. *Electromagnetic Metamaterials: Transmission Line Theory and Microwave Applications*. John Wiley & Sons Inc. , 2005.
- [25] Dworsky, L. N. *Modern transmission line theory and applications*. Vol. 260. John Wiley & Sons Inc., 1979.
- [26], [27] Freedman, Young &. *University Physics. 12th Edition*. Pearson- Addison Wesley, 2008.
- [28], [34] Pozar, D. M. *Microwave Engineering*. New York: John Wiley & Sons, Inc., 1998.
- [29] Choma, J. & Chen W. K. *Feedback networks: Theory and circuit applications*. World Scientific, 2007.
- [30] Gao, C. and X. D. Xiang. "Quantitative Microwave Near-field Microscopy of Dielectric Properties." *Review of Scientific Instruments* 69.11 (1998): 3846-3851.
- [31] Montgomery, C. G., R. H. Dicke and E. M. (Eds.) Purcell. *Principles of microwave circuits No. 25*. IET, 1948.
- [32] Kaiser, K. L. "Electromagnetic Compatibility Handbook." CRC press, 2004. 7.71-7.72.